J. Fluid Mech. (2005), *vol.* 543, *pp.* 57–92.
doi:10.1017/S0022112005005975 Printed in the United Kingdom

Dynamics of field-amplified sample stacking

By RAJIV BHARADWAJ[1] AND JUAN G. SANTIAGO[2]

[1]Department of Chemical Engineering, Stanford University, Stanford, CA 94305, USA

[2]Department of Mechanical Engineering, Stanford University, Building 530, Stanford, CA 94305, USA
juan.santiago@stanford.edu

(Received 31 January 2004 and in revised form 11 April 2005)

Field-amplified sample stacking (FASS) uses conductivity gradients and resulting non-uniform electromigration fluxes to effect concentration increases of analyte ions. For cases where the initial sample concentration is much smaller than the background electrolyte (BGE) concentration, the ideal maximum concentration enhancement is equal to γ, the ratio of conductivity of the sample solution to that of the BGE. However, in practice both molecular diffusion and convective dispersion limit concentration enhancement. We present a theoretical and experimental study of concentration enhancement using FASS. We model the FASS process as electromigration, diffusion, and advection of two background electrolyte ions and multiple sample species across a known initial concentration gradient. Regular perturbation methods and a generalized Taylor dispersion analysis are used to derive area-averaged species conservation and electric field equations. The model predicts the spatial and temporal development of background electrolyte concentration field, electric field, and sample-ion distribution of the FASS process. We have validated this model using on-chip FASS experiments. We use an acidified poly(ethylene oxide) (PEO) coating to minimize dispersion due to electro-osmotic flow (EOF), and thereby evaluate the low- (but finite) dispersion regime of most interest. We have used CCD-based quantitative epifliuorescence imaging to quantify unsteady concentration fields and validate the model. This experimentally validated model is useful in developing optimal designs of sample stacking assay devices.

1. Introduction

Sensitivity to low analyte concentrations is a crucial challenge in the development of robust miniaturized bioanalytical devices. Field-amplified sample stacking (Burgi & Chien 1991) is a promising method of achieving increased sensitivity for on-chip assays in a scheme that is easily integrated with electrophoretic separation techniques (Jung, Bharadwaj & Santiago 2003; Yang & Chien 2001). FASS is typically used as a preconcentration step that occurs prior to the electrophoretic separation of analyte ions. In the first phase of such experiments, sample ions are preconcentrated using heterogeneous electrolyte solutions. In the second phase, the concentrated analyte is subjected to electrophoretic separation in a homogenous electrolyte solution. Such experiments have been performed using microchips by Yang & Chien (2001) and Lichtenberg, Verpoorte & Rooij (2001). Our focus, in this paper, is the analysis of the preconcentration step involving FASS. The design and optimization of the second step of electrophoretic separation process in homogenous electrolytes has been described by Bharadwaj, Santiago & Mohammadi (2002).

The transport phenomenon associated with FASS is in general a complex coupling of convective-diffusion, electrostatics, and electrokinetics along with the unsteady effects associated with the response of the electrical double layer to varying bulk ion concentrations. The detailed understanding of the process dynamics is important for optimization of high-sensitivity systems. Bier *et al.* (1983) developed a comprehensive mathematical model to study a variety of electrophoretic processes using numerical simulations. However, effects of electro-osmotic flow (EOF) were not taken into account in their work. The effects of EOF on stacking and separation are very important to studies of FASS as even slight EOF couples with axial conductivity gradients to generate internal pressure gradients. These internal pressure gradients disperse the sample and thereby limit the practically achievable concentration enhancement. Burgi & Chien (1991) developed a simple algebraic model to study the effects of dispersion on stacking efficiency. In their model, the classic Taylor dispersion coefficient (Taylor 1953) was used to quantify dispersion due to non-uniform EOF. More recently, Sounart & Baygents (2001) developed a general multi-component model for electro-osmotically driven separation processes. They performed two-dimensional numerical simulations to study the effect of electro-osmosis on the concentration distributions in FASS. Their simulations demonstrate that in a frame of reference moving with the bulk flow velocity, the velocity field exhibits regions of recirculating flow in the vicinity of the conductivity gradients. Their results show that the recirculating flow can drastically reduce the efficiency of sample stacking. For high-sensitivity applications, dispersion due to EOF mismatch should be minimized. One approach for dispersion reduction is suppression of EOF by coating channel walls with water-soluble polymers (Horvath & Dolnik 2001). Yang & Chien (2001) and Jung *et al.* (2003) have performed FASS under suppressed EOF conditions to achieve 100 and 1000 fold signal increase respectively.

In this paper we describe experimental and theoretical investigation of FASS dynamics. Our approach for quantifying dispersion effects is to combine area-averaged convective diffusion equations with regular perturbation methods to provide a simplified set of equations for this complex process. Such simplified models provide useful insight into the physics of the process and lead to the identification of key parameters that can be used to develop optimization strategies for experiments. These models also provide a method of achieving computationally efficient calculations that are useful to optimization and design efforts. We use full-field epifluorescence imaging to quantify the spatial and temporal distribution of unsteady concentration fields in FASS and to validate our model.

The paper is organized as follows. In the next section the physical principle behind FASS and the general governing equations are described. We then describe analytical and numerical models for FASS dynamics. The analytical model describes the non-dispersive electromigrational dynamics of three-ion FASS, and the semi-analytical dispersion model encompasses a generalized Taylor dispersion analysis that includes the effects of molecular diffusion and advective dispersion. Finally, we describe the experimental results and their comparison with the mathematical model.

2. Theory

The principle behind field-amplified sample stacking (FASS) is shown schematically in figure 1(*a*). An axial gradient in ionic conductivity (and therefore electric field) is achieved by preparing the sample in an electrolyte solution of lower concentration than the background electrolyte (BGE). Upon application of an axial potential

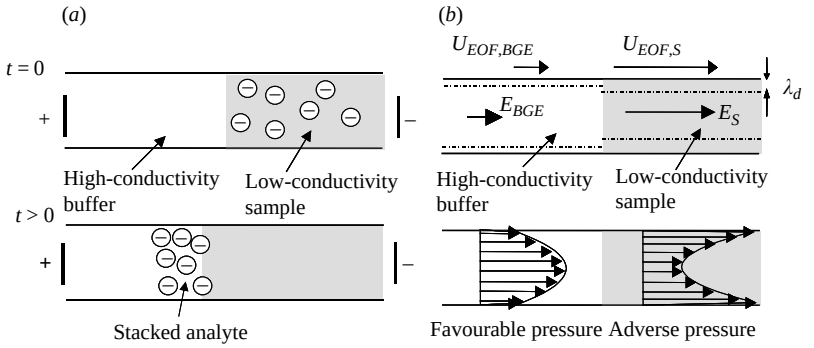

FIGURE 1. (*a*) Schematic showing FASS of anionic species in the absence of EOF. A gradient in the background electrolyte ion concentration is established with the sample in the low conductivity zone. Upon application of an electric field, the axial gradient in conductivity results in an electric field gradient. Since area-averaged current density is uniform along the axis of the channel, the low conductivity section is a region of high electric field, and the region of high conductivity contains relatively low electric field. As sample ions exit the high field/high electrophoretic velocity region and enter the low velocity region, they locally accumulate and increase in concentration. (*b*) Stacking in the presence of EOF. Gradients in conductivity generate axial variation in electric field and electro-osmotic mobility. The system generates internal pressure gradients that tend to disperse sample.

gradient, the sample region acts as a high-electrical-resistance zone in series with the rest of the channel and a locally high electric field is generated within the sample zone. Under the influence of electric field, sample ions migrate from the high to low drift velocity region. This leads to a local accumulation or 'stacking' of sample ions near the interface between regions of high and low conductivity. This stacking increases sample concentration and results in an increased signal. (Note that, in the absence of a conductivity gradient, a spatial gradient in mobility would also work.) The process depicted in figure 1(*a*) is for an idealized case where diffusion and advection are neglected. Figure 1(*b*) shows a more realistic system where finite electro-osmotic flow is present. The gradient in the electrolyte concentration required for stacking leads to a gradient in electric field and electro-osmotic mobility. This causes a mismatch of electro-osmotic velocity and hence generation of a pressure gradient (consistent with the continuity constraint). The pressure gradient tends to disperse the concentration fields and thereby lower the efficiency of stacking.

2.1. *Problem formulation*

In this section we describe the general governing equations for the evolution of ionic species in an FASS process at an single electrolyte–electrolyte interface (figure 1). The single interface configuration models the field-amplified sample injection (FASI) (Chien & Burgi 1991) and the large-volume sample stacking (LVSS) (Chien & Burgi 1992) techniques used in capillaries and microchip-based assays. We consider a system of $N+2$ fully ionized ions. Ions A and B refer respectively to a cation and anion which represent the background buffer ions. We define $C_{S,j}$ to be the concentration of the jth sample ion in a population of N sample ions. For dilute electrolyte solutions, the flux contributions from molecular diffusion, electromigration, and convection can be linearly superposed and the species conservation equation can be written as (Probstein 1994)

$$\frac{\partial C_i}{\partial t} + \boldsymbol{u}\cdot\nabla C_i = -z_i \nu_i F \nabla\cdot(C_i \boldsymbol{E}) + D_i \nabla^2 C_i, \qquad i = A, B, S_j. \tag{2.1}$$

Here, C_i is the concentration of ionic species i (e.g. C_A refers to concentration of buffer cation A), D_i, is the molar diffusivity of species i, ν_i is the electromigration mobility, z_i is the valence number, F is Faraday's constant, $\boldsymbol{u}$ is the fluid velocity, and $\boldsymbol{E}$ is electric field.

In electrokinetic flow physics, applied electric fields couple with conductivity gradients (as in FASS) and in lead to the generation of net charge in the bulk liquid. However, this charge density is negligible compared to the total background ion concentration. We can therefore assume that the solution is approximately electrically neutral everywhere except in the electrical double layer, so that

$$z_A C_A + z_B C_B + \sum_{j=1}^{N} z_{S,j} C_{S,j} \approx 0. \tag{2.2}$$

This approximation is discussed in detail elsewhere (Probstein 1994; Lin *et al.* 2003).

The low-Reynolds-number microchannel flows of interest here are described by the Stokes equations of motion with an additional term for bulk charge density of the form

$$\nabla P = \mu \nabla^2 \boldsymbol{u} + \rho_E \boldsymbol{E}; \quad \nabla \cdot \boldsymbol{u} = 0 \tag{2.3}$$

where μ is the fluid viscosity and ρ_E is the volume charge density. The charge density term in the momentum equation can in general describe electric body forces both within the electrical double layer and in the bulk liquid (outside of the double layer). We shall describe each of these two flow regions in order.

Outside of the double layer, the term $\rho_E \boldsymbol{E}$ in the momentum equation accounts for Columbic body forces associated with net charge in the bulk liquid. For electro-osmotic flows (and typical FASS systems) this force density can be shown to be much smaller than local internally generated pressure gradients associated with electro-osmotic mobility gradients in the channel. This approximation is discussed in detail in the Appendix and leads to a momentum balance of the form $\nabla p \approx \mu \nabla^2 \boldsymbol{u}$ that will be applied here to describe the dynamics of the bulk liquid.

The electric body force within the electric double layer gives rise to a thin boundary layer supporting high shear stress near the wall. In typical electro-osmotic flows in microchannels, the characteristic double layer thickness (the Debye length), λ_d, is much smaller than the channel depth, and EOF can therefore be modelled as bounded by a slip surface which is parallel to and within a few Debye lengths of the wall. This treatment of the double-layer physics results in a boundary condition where slip velocity is everywhere proportional to local electric field (and local zeta potential), but which can also support a finite shear stress. This approximation is described in detail by Santiago (2001). In this approach, the electrical double layer need not be treated in detail and the physical forces within the electrical double layer can be replaced by a slip surface with a local velocity of the form that is everywhere proportional to local field and local zeta potential:

$$u_{slip} = -\left.\frac{\varepsilon_o \varepsilon_r \zeta(x,t) E_x(x,t)}{\mu}\right|_{y=\pm d}. \tag{2.4}$$

where ε_o is the permittivity of free space and ε_r is the relative permittivity. Santiago (2001) describes the conditions for this approximation. This relation can be thought of as a Helmholtz–Smoluchowski equation slightly generalized to the case of non-uniform fields and zeta potential.

Zeta potential, ζ, is in general a function of local ionic concentration and pH (Hunter 1981; Scales, Grieser & Healy 1992) In typical FASS experiments, pH can be assumed to be constant as chemical buffers with sufficiently high concentrations are typically used. We use the following model for the concentration dependence of the zeta potential:

$$\zeta = aC^b. \tag{2.5}$$

The exponent and pre-factor depend on the chemistry of the channel surface and the electrolyte solution. A typical range of the exponent is between -0.2 and -0.3 (Scales *et al.* 1992; Yao *et al.* 2003; Sadr *et al.* 2004) In this study, we assume a value of -0.2 for the theoretical calculations. FASS dynamics in the flow regimes explored here have only a weak dependence on this parameter.

The boundary conditions on concentration and potential field are the following:

$$\left.\begin{aligned} &C_A(x=-L,t)=\gamma C_{Ao};\ C_A(x=L,t)=C_{Ao};\ \left.\frac{\partial C_A}{\partial y}\right|_{y=\pm d}=0,\\ &C_{S,j}(x=-L,t)=0;\ C_{S,j}(x=L,t)=C_{S,jo};\ \left.\frac{\partial C_{S,j}}{\partial y}\right|_{y=\pm d}=0,\\ &\phi(x=-L,t)=\phi_o;\ \phi(x=L,t)=0;\ \left.\frac{\partial \phi}{\partial y}\right|_{y=\pm d}=0. \end{aligned}\right\} \tag{2.6}$$

Now, let s_S, s_B be the characteristic length scales over which we have significant initial sample and buffer concentration gradients respectively. For channel lengths much larger than the characteristic interface length s_S, we can assume the following initial conditions:

$$\left.\begin{aligned} C_A(x,t=0)&=\frac{C_{Ao}}{2}((1+\gamma)+(1-\gamma)\mathrm{erf}(x/s_B)),\\ C_{S,j}(x,t=0)&=\frac{C_{S,jo}}{2}(1+\mathrm{erf}(x/s_S)). \end{aligned}\right\} \tag{2.7}$$

Here γ is the ratio of concentration of buffer ions in the high and low conductivity regions, C_{Ao} is the buffer-ion concentration in the low-conductivity region, and $C_{S,jo}$ is the initial sample ion concentration. These initial conditions refer to FASS across a single electrolyte–electrolyte interface as depicted in figure 1. The single interface configuration models the FASI (Chien & Burgi 1991) or LVSS (Chien & Burgi 1992) processes used in capillary-based systems. Yang & Chien (2001) and Jung *et al.* (2003) have also used a similar single electrolyte–electrolyte interface for microchip-based FASS applications. The error function profile is suggested by the solution of a simple one-dimensional diffusion solution across an initial sharp boundary, and approximates the initial conditions of a FASS experiment (prior to the application of a stacking/electrophoretic separation electric field). The boundary and initial condition for the buffer ion, B, is then fixed by the electroneutrality constraint.

The set of PDEs (equations (2.1), (2.2) and (2.3)) is coupled and strongly nonlinear and thus general analytical solutions are difficult. For example, note that the boundary condition on velocity is unsteady and coupled to the evolving, unsteady concentration field through the dependence of zeta potential on local ion density. In the next section we discuss simplifications of these general equations that enable tractable solutions and shed light on the key physical mechanics of dispersion.

3. Analytical model for ideal dynamics

FASS is essentially an electromigrational phenomenon and thus we first consider a model based purely on unsteady electromigration of two BGE ions (A^+, B^-) and one sample ion (C^-). This idealization helps describe the basic wave-like propagation and steepening dynamics associated with FASS and can be interpreted as a study of conditions ideal for stacking. Notable past work in this area includes the seminal work of Mikkers, Everaerts & Verheggen (1979). They developed a one-dimensional model based on Kohlrausch's regulating function (Kohlrausch 1897) to study concentration distributions during electrophoresis. They presented an analytical solution for the asymptotic (long-time) concentration distribution for the case of pure electromigration, neglecting diffusion and advection. Our model is similar to that of Mikkers *et al.* (1979) but with the distinction (and associated generalization) that we focus on both the short-term and long-term behaviour of the FASS concentration field and that we are here interested in the stacking dynamics across a single interface in the ionic concentration distribution of the BGE. We assume that the concentration varies only along the axial direction. A steady bulk current density (total current per unit channel cross-sectional area), j_o, is applied in the axial direction. Under these assumptions the simplified governing equations are

$$\frac{\partial C_i}{\partial t} = -z_i F \nu_i \frac{\partial}{\partial x}(C_i E); \quad i = A, B, C \tag{3.1}$$

and

$$\sum z_i C_i = 0. \tag{3.2}$$

These coupled and nonlinear equations govern the concentration and electric field distribution. After algebraic manipulation, equations (3.1)–(3.2) can be reduced to the following:

$$E(x,t) = \frac{j_o}{\sigma(x,t)}. \tag{3.3}$$

Here, $\sigma(x,t) = F^2 \sum z_i^2 \nu_i C_i$, is the electrical conductivity distribution. Further, the following relation can be obtained:

$$\frac{\partial (pC_A(x,t) + qC_C(x,t))}{\partial t} = 0 \Rightarrow pC_A(x,t) + qC_C(x,t) = f(x) \tag{3.4}$$

where $p = z_A - z_B(\nu_B/\nu_A)$ and $q = z_C - z_B(\nu_B/\nu_C)$. The numerical value of $f(x)$ is determined, for all times, by the initial conditions. This function is analogous to Kohlrausch's regulating function mentioned earlier.

Finally, the sample ion distribution is governed by

$$\frac{\partial C_C}{\partial t} = -z_C \frac{j_o}{F} \frac{\partial}{\partial x} \left(\frac{\nu_C C_C}{z_A \nu_A f(x) + C_C h} \right) \tag{3.5}$$

where $h = (z_C \nu_C - z_B \nu_B)(z_C - z_A(\nu_A/\nu_C))$.

The conservation equation (3.5) for sample C is a nonlinear wave equation where the wave velocity depends on the concentration distribution. This is clearer when we apply the following variable transformation:

$$\phi \equiv \frac{C_C \nu_C}{z_A f(x) \nu_A + C_C h} \tag{3.6}$$

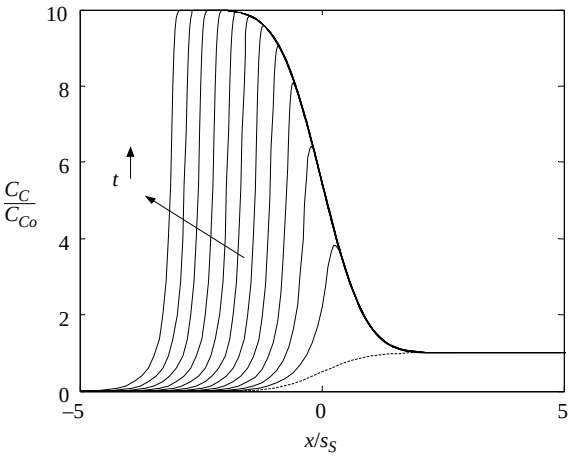

FIGURE 2. Plot of concentration profiles during stacking across a single interface. The dotted curve represents the initial sample-ion profile. The peak intensity increases in time until a saturation value equal to γ is achieved. The variance of the stacked sample ion also increases with time as sample accumulates in the high-conductivity region. The applied current density is $1500\,\mathrm{A\,m^{-2}}$, $\gamma = 10$, $s_S = 50\,\mu\mathrm{m}$, $C_{Ao}/C_{Co} = 1000$ and the time between successive plots is 75 ms.

so that equation (3.5) reduces to

$$\phi_t + \frac{j_o z_c \nu_A (\nu_C/\nu_A - h\phi)^2}{z_A \nu_C f(x) F}\phi_x = 0. \tag{3.7}$$

This PDE is solved analytically using the method of characteristics. The characteristics are of the form

$$\int f(x)\,\mathrm{d}x - \frac{j_o z_c \nu_A (\nu_C/\nu_A - h\phi)^2 t}{z_A \nu_C F} = C_1 \tag{3.8}$$

and

$$\phi = C_2. \tag{3.9}$$

Due to the nonlinearity of the problem, the analytical solution is implicit but can be easily developed along the characteristics:

$$\phi = G\left(\int f(x)\,\mathrm{d}x - \frac{j_o z_c \nu_A (\nu_C/\nu_A - h\phi)^2 t}{z_A \nu_C F}\right) \tag{3.10}$$

where the function G is determined by the sample ion initial condition.

In figures 2–5 we consider results from the electromigration model. For the results shown in figures 2–5, the absolute mobility value of all the three ions is equal to $5.2 \times 10^{-8}\,\mathrm{m^2\,V^{-1}\,s^{-1}}$. Figure 2 shows the concentration profiles of the sample-ion solution as a function of position and time. The corresponding electric field profiles are plotted in figure 3. As in most FASS situations, we consider a case where the BGE-ion to sample-ion concentration ratio is large (set equal to 1000 here). Due to this high value of the initial BGE-to-sample-ion concentration ratio, the electric field distribution in the channel is nearly constant. The relatively high-concentration BGE ions govern the background conductivity and follow binary electrolyte dynamics. This aspect of the solution will be exploited in the next section to develop a regular perturbation analysis of the general governing equations for the case of sample ion concentrations much lower than the concentrations of the BGE.

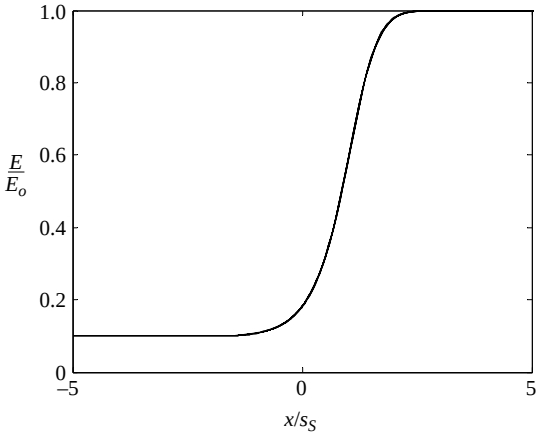

FIGURE 3. Electric field profiles under the same conditions as the plot in figure 2 and for a total evolution time of 0.825 s. The electric field distribution in nearly time-invariant.

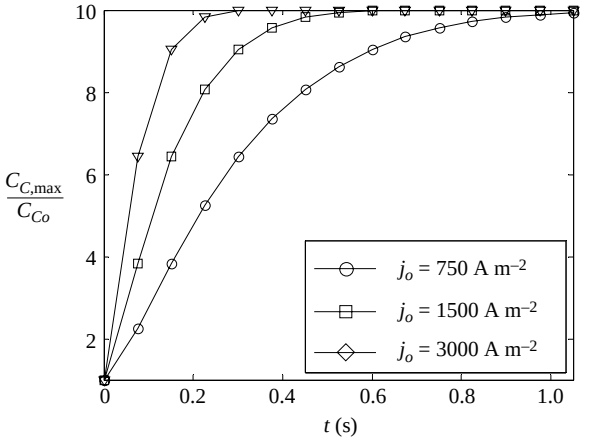

FIGURE 4. Effect of current density on the rate of concentration increase. The parameter values for the curves are as in figure 2.

In this idealized, hyperbolic case of FASS, the high field inside the sample region drives a large electromigration flux of negatively charged sample ions into the lower electric field region. The flux of ions away from the interface (on the left-hand side of the interface within the high-conductivity region), however, is relatively small. There is therefore a local accumulation of sample ions in the region of the interface. The sample concentration increases until the following flux balance is achieved:

$$z_C F \nu_C C_C E|_S = z_C F \nu_C C_C E|_{BGE} \tag{3.11}$$

or

$$\frac{C_{Stacked}}{C_{Initial}} = \frac{E_S}{E_{BGE}} = \gamma. \tag{3.12}$$

The sample-ion distribution develops as a travelling wave with peak height increasing in time until the concentration enhancement reaches a maximum value of γ. Due to the nature of the single-interface initial conductivity gradient (and of the initial sample concentration) the variance of the stacked sample increases indefinitely with time. Figure 4 shows the effect of current density, and therefore electric field, on

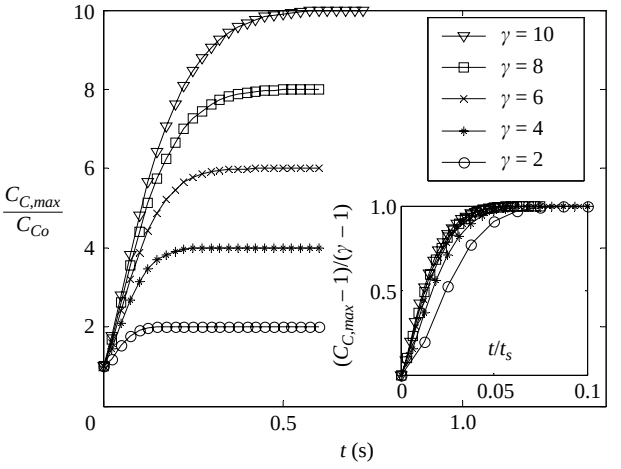

FIGURE 5. Concentration increase versus time as a function of γ for a current density of $1500\,\mathrm{A\,m^{-2}}$, $s_S = 50\,\mu\mathrm{m}$, and $C_{Ao}/C_{Co} = 1000$. Inset: data scaled as suggested by the control volume analysis.

the stacking dynamics. The parameter, $C_{C,max}$, is the maximum value of sample ion concentration at a given time step. The electric field magnitude does not affect the maximum concentration achieved, but the rate of stacking is proportional to electric field magnitude. Figure 5 shows the effect of γ on the rate of concentration increase given a fixed current density. The concentration increases roughly exponentially at first and then saturates at a value set by γ. The time to achieve the theoretical maximum concentration enhancement is directly proportional to γ.

We can use a simple control volume analysis to derive an approximate solution to the stacking dynamics. A control volume is defined such that its left and right boundaries are well away from the BGE interface region and the region of accumulated sample. A mass balance yields

$$\frac{\mathrm{d}C_C}{\mathrm{d}t} = \frac{F j_o z_C}{\sigma_o s_S}\left(C_{C_o} - \frac{C_C(t)}{\gamma}\right) \tag{3.13}$$

where the left-hand side is accumulation and the right-hand side is the rate of influx minus the rate of outflux. Rearranging this relation and integrating over time, a closed-form solution can be derived for the evolution of peak concentration as follows:

$$\frac{C_C(t)/C_{C_o} - 1}{\gamma - 1} = 1 - \exp\left(-\frac{j_o \nu_C F z_C}{s_S \sigma_o \gamma} t\right). \tag{3.14}$$

The normalization on the left-hand side of this expression can be interpreted as the efficiency of the stacking process. This relation explicitly shows that the relevant time scale of this process is proportional to γ and of the form

$$t_{scale} \sim \frac{s_S \sigma_o \gamma}{j_o \nu_C F z_C}. \tag{3.15}$$

For a given current density, therefore, longer analysis time is required to achieve higher concentration enhancement. We have used the above scaling to replot the data shown in figure 5. The inset shows that the collapse of the data is fairly good although not perfect.

4. Dispersion model for FASS

4.1. *Regular perturbation analysis*

The electromigration model developed above provides a description of the ideal FASS dynamics in the absence of dispersive forces. Next, we develop a model to investigate the effects of molecular diffusion and convective dispersion on the performance of practical FASS systems. The general set of PDEs is coupled and strongly nonlinear. However, since the concentration of sample ions is much smaller than the buffer ions (typically μM sample-ion concentration or less versus order 1 mM buffer-ion concentration) we employ a regular perturbation technique to decouple the buffer- and sample-ion concentration fields. We define the expansion parameter as the ratio of the initial sample- and buffer-ion concentration in the low-conductivity region:

$$\varepsilon = \frac{C_{S,jo}}{C_{Ao}}. \tag{4.1}$$

Typical values of this parameter are order 10^{-3} or less. The dependent variables in the problem, Y_i, are expanded as

$$Y_i = Y_i^0 + \varepsilon Y_i^1 + \varepsilon^2 Y_i^2 + \cdots. \tag{4.2}$$

These series expansions are substituted for the variables in the governing equations (i.e. C_A, C_B, $C_{S,j}$, E, and $\boldsymbol{u}$) and terms of equal power in ε are equated. The zeroth-order equation set is then

$$\frac{\partial C_A^0}{\partial t} + \boldsymbol{u}^0 \cdot \nabla C_A^0 = \overline{D}\nabla^2 C_A^0;\ \overline{D} = \frac{z_A \nu_A D_B - z_B \nu_B D_A}{z_A \nu_A - z_B \nu_B}, \tag{4.3}$$

$$C_B^0 = -C_A^0 (z_A / z_B), \tag{4.4}$$

$$C_{S,j}^0 = 0; j = 1 : N, \tag{4.5}$$

$$(z_A \nu_A - z_B \nu_B) F \nabla \cdot \left(C_A^0 \nabla \phi^0\right) + (D_A - D_B)\nabla^2 C_A^0 = 0, \tag{4.6}$$

$$\left.\begin{aligned} \nabla p^0 &= \mu \nabla^2 \boldsymbol{u}^0;\ \nabla \cdot \boldsymbol{u}^0 = 0, \\ u_{slip}^0 &= -\frac{\varepsilon_o \varepsilon_r \zeta^0 E_x^0}{\mu}\bigg|_{y=\pm d} \end{aligned}\right\} \tag{4.7}$$

At zeroth order, the sample-ion concentration is negligible and thus the buffer ions follow binary electrolyte dynamics as described in equation (4.3). The detailed derivation of the effective diffusion coefficient, $\overline{D}$, is documented elsewhere (Probstein 1994). The buffer ions control the electric field distribution as dictated by the conservation of current equation (4.6). The first-order sample-ion distribution is given by

$$\frac{\partial C_{S,j}^1}{\partial t} + \boldsymbol{u}^0 \cdot \nabla C_{S,j}^1 = z_{S,j} \nu_{S,j} F \nabla \cdot \left(C_{S,j}^1 \nabla \phi^0\right) + D_{S,j} \nabla^2 C_{S,j}^1. \tag{4.8}$$

By virtue of their small concentration, sample ions act as a 'passive scalar' in the electric and velocity field set up by the buffer ions. Note that Levich (1942) has also discussed a similar simplification of species conservation equations in the context of electrochemical processes at electrodes. The concentration distribution of individual sample species can be calculated independently of the other (low-concentration) sample species using equation (4.8). The overall electrophoregram can then be generated by linear superposition of each sample species concentration field. As described in § 6, our approach can therefore be used to calculate stacking and

separation dynamics of multiple sample ions. The solution to these zeroth- and first-order problems are explored below with the aid of an area-averaging approach that yields solutions directly comparable to experimental observations.

4.2. *Dispersion calculation via area averaging*

In most electrophoretic experiments, the quantity of practical interest is the cross-sectional-area-averaged concentration distribution of sample ions. This quantity is, for example, proportional to the measured signal intensity of line-of-sight optical integrators such as point-wise fluorescence detectors, transmitted-mode absorption detectors, and width-averaged electrophoregrams from CCD arrays. This signal determines the key detectability constraints of electrophoretic separations (Bharadwaj *et al.* 2002). In this section, we therefore develop cross-sectional-area-averaged transport equations applicable to FASS problems. The concept of cross-section averaging of governing equations for dispersion calculations was first described by Taylor (1953) and further established by Aris (1956). Another example is the work of Saville (1990) who used Taylor dispersion analysis to study the effect of a unidirectional and unvarying velocity profile on the structure of steady isotachophoresis boundaries.

Brenner & Edwards (1993) have developed a formal generalized Taylor dispersion theory that extends the Taylor-dispersion-type analysis to a much broader class of dispersive phenomena than the Poiseuille flow dispersion analysis investigated by Taylor. One restriction on Brenner's generalized Taylor dispersion analysis is that the constitutive equations should be linear with respect to concentration of the scalar. The governing equations for FASS are nonlinear and hence direct application of generic analysis is not possible. Our approach for quantifying dispersion effects is to use area averaging with order-of-magnitude estimates to obtain cross-section-averaged quantities. Past work pertinent to the present study includes that of Stone & Brenner (1999) and Sauber, Locke & Arce (1995). Stone & Brenner applied area averaging together with order-of-magnitude estimates and formal generalized Taylor dispersion theory to calculate effective dispersion coefficient for flows with streamwise variations of mean velocity. Sauber *et al.* employed area-averaging techniques to study the effects of axial and orthogonal electric fields on solute transport in Poiseuille flow.

In the next four subsections, we apply an area-averaging approach to the coupled convective diffusion/electromigration problem of FASS. We describe the simplification and solution approach to the velocity field, the buffer-ion equation, the potential field, and the ion concentration field. We then present a non-dimensionalization and scaling of the problem and summarize our method of solution.

4.2.1. *Velocity field*

We consider a rectangular-cross-section channel of length $2L$, depth $2d$ and width $2w$. The channel is assumed to be long and thin, $L/d \gg 1$, with small depth-to-width aspect ratio, $d/w \ll 1$. This is a simplified description of a type of wide/shallow microchannel geometry found in many on-chip electrophoresis devices. (Note that a similar solution method can be applied readily to the problem of cylindrical channels and other cross-sectional area shapes provided solutions of velocity fields are available.) The velocity field is coupled to the buffer-ion concentration only through the wall boundary condition. The unsteady forces associated with the development of the unsteady concentration field are neglected so that we consider only a quasi-steady Stokes equation formulation of the form of equation (2.3). Specifically, we consider the case where the Reynolds number based on electro-osmotic flow bulk velocity and

channel depth is small as is the product of Reynolds and Strouhal numbers (Santiago 2001).

The Stokes equations with slip condition can be solved analytically using finite Fourier transforms. Andersen & Idol (1985) have described such a solution for electro-osmosis in a cylindrical pore with non-uniform surface charge. Here, we perform a similar analysis in a two-dimensional rectangular-cross-section channel with non-uniform axial field and surface potential. The analysis presented here is valid in the limit $L/d \to \infty$ and $d/\lambda_d \to \infty$. In the calculations reported in this section, the cross-section-averaged quantities are defined as $\langle \cdots \rangle = (2d)^{-1} \int_{-d}^{d} \ldots \mathrm{d}y$.

The stream function formulation is used for the Stokes equation:

$$\nabla^4 \psi = 0. \tag{4.9}$$

This equation is solved using finite Fourier transforms and the solution is

$$\psi = \overline{\psi}(y, 0) + 2\left(\sum_{m=1}^{\infty} \overline{\psi}_C(y, m)\cos(\alpha_m x) + \overline{\psi}_S(y, m)\sin(\alpha_m x)\right) \tag{4.10}$$

where

$$\alpha_m = \frac{m\pi}{L}. \tag{4.11}$$

An overbar denotes the cosine and sine transforms:

$$\left.\begin{aligned} \overline{\psi}_C(y, m) &= \frac{1}{2L}\int_{-L}^{L} \psi(y, x)\cos\left(\frac{m\pi}{L}x\right)\mathrm{d}x, \\ \overline{\psi}_S(y, m) &= \frac{1}{2L}\int_{-L}^{L} \psi(y, x)\sin\left(\frac{m\pi}{L}x\right)\mathrm{d}x. \end{aligned}\right\} \tag{4.12}$$

The analysis results in the following velocity profile:

$$\left.\begin{aligned} u_x(x, y, t) &= \langle u\rangle + \left(3\left(\frac{y}{d}\right)^2 - 1\right)\sum_{m=1}^{\infty} \overline{u}_C(m, t)\cos(\alpha_m x) + \overline{u}_S(m, t)\sin(\alpha_m x), \\ u_y(x, y, t) &= y\left(\left(\frac{y}{d}\right)^2 - 1\right)\sum_{m=1}^{\infty} -\alpha_m \overline{u}_C(m, t)\sin(\alpha_m x) + \alpha_m \overline{u}_S(m, t)\cos(\alpha_m x). \end{aligned}\right\} \tag{4.13}$$

The slip-velocity transforms are defined as

$$\left.\begin{aligned} \overline{u}_C(m, t) &= \frac{1}{2L}\int_{-L}^{L} u_{slip}(x, t)\cos(\alpha_m x)\,\mathrm{d}x, \\ \overline{u}_S(m, t) &= \frac{1}{2L}\int_{-L}^{L} u_{slip}(x, t)\sin(\alpha_m x)\,\mathrm{d}x. \end{aligned}\right\} \tag{4.14}$$

Following the work of Andersen & Idol (1985) the area-averaged bulk velocity, can be expressed as an axial integral of the slip velocity:

$$U_{bulk} = \langle u\rangle = \frac{1}{2L}\int_{-L}^{L} u_{slip}(x, t)\,\mathrm{d}x. \tag{4.15}$$

The axial velocity has two components: the bulk average velocity, $\langle u\rangle\,\hat{\boldsymbol{i}}$, and the deviation velocity, $\boldsymbol{u} - \langle u\rangle\,\hat{\boldsymbol{i}}$. The bulk velocity component simply convects the solute downstream without dispersion. The unsteady secondary flow, $\boldsymbol{u} - \langle u\rangle\,\hat{\boldsymbol{i}}$, varies both in the transverse and streamwise directions and causes dispersion of the solute.

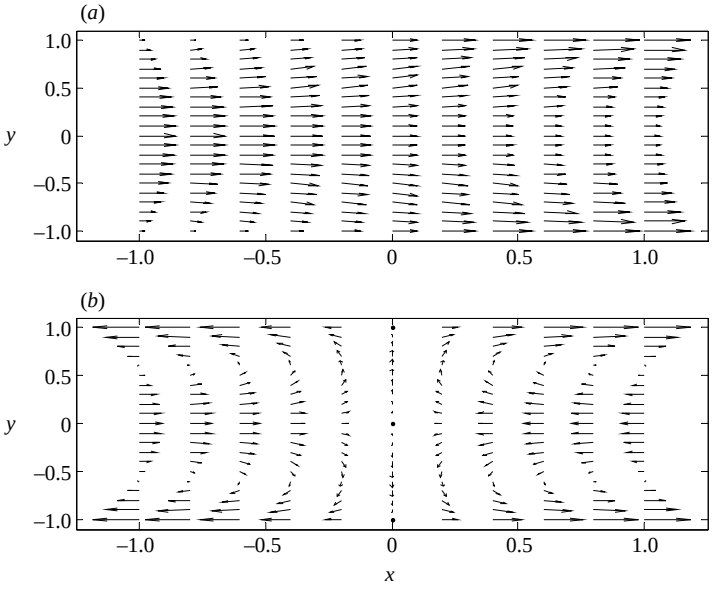

FIGURE 6. Instantaneous FASS vector fields. (*a*) Vector field in a reference frame stationary with respect to the laboratory showing the two-dimensional transition region between favourable and adverse pressure gradients. (*b*) Vector field in a reference frame moving with the bulk average velocity. This secondary flow pattern leads to dispersion of the sample ions. The parameters used for this plot are $Pe = 100$, $\gamma = 5$, $\alpha = 1$, and $\delta = 10$. In both cases, the centre of the buffer-ion concentration gradient (i.e. the inflection point in the axial conductivity profile) coincides with $x = 0$.

Figure 6 shows an instantaneous velocity vector field for the initial conditions given by equation (2.7). Away from the interface, favourable and adverse pressure gradients are observed in the high- and low-conductivity regions, respectively. Near the interface, a two-dimensional transition region exists over which the pressure gradient changes direction. This two-dimensional region occupies a region of the channel with a length on the order of s_B. For times shorter than the characteristic advection time ($t \ll L/U_{bulk}$) and sharp gradients ($s_S/L \ll 1$), the axial integrals of velocity in equations (4.14) and (4.15) will vary slowly, and hence these axial integrals can be assumed to be constant. Thus, the velocity profile can be assumed quasi-steady and expressed as

$$u_x(x,t) = \langle u\rangle + \left(3\left(\frac{y}{d}\right)^2 - 1\right)\sum_{m=1}^{\infty} \overline{u}_C(m, t=0)\cos(\alpha_m(x - \langle u\rangle t)) + \overline{u}_S(m, t=0)\sin(\alpha_m(x - \langle u\rangle t)) \quad (4.16)$$

and

$$u_y(x,t) = y\left(\left(\frac{y}{d}\right)^2 - 1\right)\sum_{m=1}^{\infty} -\alpha_m\overline{u}_C(m, t=0)\sin(\alpha_m(x - \langle u\rangle t)) + \alpha_m\overline{u}_S(m, t=0)\cos(\alpha_m(x - \langle u\rangle t)) \quad (4.17)$$

where

$$\langle u\rangle = \frac{1}{2L}\int_{-L}^{L} u_{slip}(x, t=0)\,\mathrm{d}x \quad (4.18)$$

and all axial integrals of slip velocity are based on initial conditions. This important approximation simplifies the nonlinear coupling between the velocity field and the concentration distribution and facilitates a dispersion analysis.

In the next part of the analysis, we will assume that the effect of transverse velocity on axial dispersion is negligible, which implies that axial dispersion is predominantly due to axial velocity components. That is, although transverse velocities exist, they do not contribute strongly to the development of the area-averaged concentration. Note that this assumption, although useful and accurate as we shall see, can probably be relaxed by carrying out a dispersion analysis for the two-dimensional velocity field using the formal generalized Taylor dispersion theory described by Brenner & Edwards (1993) under the current assumptions.

4.2.2. *Averaged buffer ion equation*

Under the assumptions described above, the buffer-ion concentration field evolves according to the following convective–diffusion equation:

$$\frac{\partial C_A^0}{\partial t} + u_x^0(x, y)\frac{\partial C_A^0}{\partial x} \approx \overline{D}\left[\frac{\partial^2 C_A^0}{\partial x^2} + \frac{\partial^2 C_A^0}{\partial y^2}\right]. \tag{4.19}$$

Next, we carry out a dispersion analysis by substituting the following:

$$\left.\begin{aligned} C_A^0(x, y, t) &= \overline{C}_A^{\,0}(x, t) + C_A'^0(x, y, t), \\ u_x^0(x, y) &= \langle u\rangle^0 + u_x'^0(x, y, t), \end{aligned}\right\} \tag{4.20}$$

where the barred quantities are the cross-section-averaged variables and the primed quantities are deviation variables.

The deviation term for axial velocity is

$$u_x'^0(x, y, t) = \left(3\left(\frac{y}{d}\right)^2 - 1\right)\sum_{m=1}^{\infty} \overline{u}_C^0(m, t=0)\cos(\alpha_m(x - \langle u\rangle^0 t)) + \overline{u}_S^0(m)\sin(\alpha_m(x - \langle u\rangle^0 t)). \tag{4.21}$$

After substituting equation (4.20) in equation (4.19) and expanding, we have

$$\frac{\partial \overline{C}_A^{\,0}}{\partial t} + \frac{\partial C_A'^0}{\partial t} + \langle u\rangle^0\frac{\partial \overline{C}_A^{\,0}}{\partial x} + \langle u\rangle^0\frac{\partial C_A'^0}{\partial x} + u_x'^0\frac{\partial \overline{C}_A^{\,0}}{\partial x} + u_x'^0\frac{\partial C_A'^0}{\partial x} = \overline{D}\left[\frac{\partial^2 \overline{C}_A^{\,0}}{\partial x^2} + \frac{\partial^2 C_A'^0}{\partial x^2} + \frac{\partial^2 C_A'^0}{\partial y^2}\right]. \tag{4.22}$$

Next, we take the cross-section average of this equation and the only non-zero components are

$$\frac{\partial \overline{C}_A^{\,0}}{\partial t} + \langle u\rangle^0\frac{\partial \overline{C}_A^{\,0}}{\partial x} + \left[\overline{u_x'^0\frac{\partial C_A'^0}{\partial x}}\right] = \overline{D}\left(\frac{\partial^2 \overline{C}_A^{\,0}}{\partial x^2}\right). \tag{4.23}$$

To derive an equation for the deviation quantity $C_A'^0$, subtract equation (4.23) from equation (4.22) to obtain

$$\frac{\partial C_A'^0}{\partial t} + \langle u\rangle^0\frac{\partial C_A'^0}{\partial x} + u_x'^0\frac{\partial \overline{C}_A^{\,0}}{\partial x} + u_x'^0\frac{\partial C_A'^0}{\partial x} = \overline{D}\left[\frac{\partial^2 C_A'^0}{\partial x^2} + \frac{\partial^2 C_A'^0}{\partial y^2}\right] + \overline{u_x'^0\frac{\partial C_A'^0}{\partial x}}. \tag{4.24}$$

We now simplify equation (4.24) by carrying out an order-of-magnitude analysis. We are interested in the case where the time scale characteristic of stacking is greater than the characteristic cross-stream diffusion time, i.e. $t \gg d^2/D_o$. This is analogous to the

'long time' constraint in the classical Taylor dispersion problem. We also assume that the channel is long and relatively thin, $L \gg d$, and recognize that the perturbation velocity is on the order of the axial-averaged bulk velocity such that $u_x'^0 = (O\langle u\rangle)$. Lastly, in the $t \gg d^2/D_o$ regime, we can assume that $C_A'^0 \ll \overline{C}_A^{\,0}$ so that

$$u_x'^0 \frac{\partial \overline{C}_A^{\,0}}{\partial x} \approx \overline{D} \frac{\partial^2 C_A'^0}{\partial y^2}. \tag{4.25}$$

This equation can be integrated to obtain $C_A'^0$ since $u_x'^0$ is known (given by equation (4.21)). This enables evaluation of the square-bracketed term in equation (4.23):

$$\overline{u_x'^0 \frac{\partial C_A'^0}{\partial x}} = -\frac{8d^2 g(x,t)}{105\overline{D}} \left(\frac{\partial}{\partial x} \left(g(x,t) \frac{\partial \overline{C}_A^{\,0}}{\partial x} \right) \right) \tag{4.26}$$

where the function $g(x,t)$ contains the Fourier series expansion and is of the form

$$g(x,t) = \sum_{m=1}^{\infty} \overline{u}_C^0(m, t=0) \cos(\alpha_m (x - \langle u\rangle^0 t)) + \overline{u}_S^0(m) \sin(\alpha_m (x - \langle u\rangle^0 t)). \tag{4.27}$$

Substituting equation (4.26) into equation (4.23) then yields the averaged equation for the buffer ion:

$$\frac{\partial \overline{C}_A^{\,0}}{\partial t} + \langle u\rangle^0 \frac{\partial \overline{C}_A^{\,0}}{\partial x} = \overline{D} \left(\frac{\partial^2 \overline{C}_A^{\,0}}{\partial x^2} \right) + \frac{8d^2 g(x,t)}{105\overline{D}} \left(\frac{\partial}{\partial x} \left(g(x,t) \frac{\partial \overline{C}_A^{\,0}}{\partial x} \right) \right). \tag{4.28}$$

The advective dispersion due to the velocity field is unsteady and varies with the axial position. The equation for the area-averaged BGE ion B follows simply from the net neutrality assumption:

$$\overline{C}_B^{\,0} = -\overline{C}_A^{\,0}(z_A/z_B). \tag{4.29}$$

In the next subsection, we shall relate the averaged potential in the channel to the area-averaged buffer-ion concentration.

4.2.3. *Averaged potential field*

For the zeroth-order problem, the potential field is given by equation (4.6), which can be re-written as

$$\frac{\partial C_A^0}{\partial x}\frac{\partial \phi^0}{\partial x} + \frac{\partial C_A^0}{\partial y}\frac{\partial \phi^0}{\partial y} + Q\frac{\partial^2 C_A^0}{\partial x^2} + Q\frac{\partial^2 C_A^0}{\partial y^2} = 0 \tag{4.30}$$

where

$$Q = \frac{D_A - D_B}{(z_A \nu_A - z_B \nu_B)F}.$$

Parameter Q has been defined solely to simplify the presentation of the above equation.

We expand the concentration and potential variables as

$$\left.\begin{aligned} C_A^0(x,y,t) &= \overline{C}_A^{\,0}(x,t) + C_A'^0(x,y,t), \\ \phi^0(x,y,t) &= \overline{\phi}^{\,0}(x,t) + \phi'^0(x,y,t). \end{aligned}\right\} \tag{4.31}$$

Upon substituting equation (4.31) into equation (4.30) and expanding, we obtain

$$\frac{\partial \overline{C}_A^{\,0}}{\partial x}\frac{\partial \overline{\phi}^{\,0}}{\partial x} + \frac{\partial C_A'^{0}}{\partial x}\frac{\partial \overline{\phi}^{\,0}}{\partial x} + \frac{\partial \overline{C}_A^{\,0}}{\partial x}\frac{\partial \phi'^{0}}{\partial x} + \frac{\partial C_A'^{0}}{\partial x}\frac{\partial \phi'^{0}}{\partial x} + \frac{\partial \overline{C}_A^{\,0}}{\partial y}\frac{\partial \phi'^{0}}{\partial y} + \frac{\partial C_A'^{0}}{\partial y}\frac{\partial \phi'^{0}}{\partial y} + Q\frac{\partial^2 \overline{C}_A^{\,0}}{\partial x^2} + Q\frac{\partial^2 C_A'^{0}}{\partial x^2} + Q\frac{\partial^2 C_A'^{0}}{\partial y^2} = 0. \quad (4.32)$$

As before, we can take the cross-section average of this equation to yield

$$\frac{\partial \overline{C}_A^{\,0}}{\partial x}\frac{\partial \overline{\phi}^{\,0}}{\partial x} + \left[\frac{\partial}{\partial x}\overline{\left(C_A'^{0}\frac{\partial \phi'^{0}}{\partial x}\right)}\right] + Q\frac{\partial^2 \overline{C}_A^{\,0}}{\partial x^2} = 0. \quad (4.33)$$

The term in square brackets is then evaluated by subtracting the cross-section-averaged equation (4.33) from equation (4.32) to obtain

$$\frac{\partial C_A'^{0}}{\partial x}\frac{\partial \overline{\phi}^{\,0}}{\partial x} + \frac{\partial \overline{C}_A^{\,0}}{\partial x}\frac{\partial \phi'^{0}}{\partial x} + \frac{\partial C_A'^{0}}{\partial x}\frac{\partial \phi'^{0}}{\partial x} + \frac{\partial \overline{C}_A^{\,0}}{\partial y}\frac{\partial \phi'^{0}}{\partial y} + \frac{\partial C_A'^{0}}{\partial y}\frac{\partial \phi'^{0}}{\partial y} + Q\frac{\partial^2 C_A'^{0}}{\partial x^2} + Q\frac{\partial^2 C_A'^{0}}{\partial y^2} - \left[\frac{\partial}{\partial x}\overline{\left(C_A'^{0}\frac{\partial \phi'^{0}}{\partial x}\right)}\right] = 0. \quad (4.34)$$

We scale the various terms using $L, d, \overline{C}_A, \overline{\phi}, RT/F$ as the characteristic scales for the axial coordinate, the transverse coordinate, concentration, potential, and Q. Again noting that $L \gg d$ and $\overline{C}_A \gg C_A'$, equation (4.34) simplifies to

$$\frac{\partial}{\partial y}\left(\overline{C}_A^{\,0}(x,t)\frac{\partial \phi'^{0}}{\partial y}\right) = \frac{\partial^2 \phi'^{0}}{\partial y^2} \approx 0. \quad (4.35)$$

This equation is subject to the boundary condition for potential,

$$\left.\frac{\partial \phi^0}{\partial y}\right|_{y=\pm d} = \left.\frac{\partial \phi'^{0}}{\partial y}\right|_{y=\pm d} = 0.$$

Since the cross-section average of the deviation variable is zero by definition, we find that $\phi'^{0} = 0$. Thus, the averaged equation for the potential field is

$$\frac{\partial}{\partial x}\left(\overline{C}_A^{\,0}\frac{\partial \overline{\phi}^{\,0}}{\partial x}\right) + Q\frac{\partial^2 \overline{C}_A^{\,0}}{\partial x^2} = 0. \quad (4.36)$$

In the next subsection, we will use this zeroth-order potential distribution to calculate the first-order sample-ion concentration distribution.

4.2.4. *Sample-ion concentration distribution*

The first-order sample-ion concentration field evolves according to a convective-diffusion–electromigration equation of the form

$$\frac{\partial C_{S,j}^1}{\partial t} + u_x^0(x,y)\frac{\partial C_{S,j}^1}{\partial x} = z_{S,j}\nu_{S,j}F\left[\frac{\partial}{\partial x}\left(C_{S,j}^1\frac{\partial \phi^0}{\partial x}\right) + \frac{\partial}{\partial y}\left(C_{S,j}^1\frac{\partial \phi^0}{\partial y}\right)\right] + D_{S,j}\left[\frac{\partial^2 C_{S,j}^1}{\partial x^2} + \frac{\partial^2 C_{S,j}^1}{\partial y^2}\right]. \quad (4.37)$$

As before, we substitute the averaged and deviation variables for concentration and potential field and carry out an analysis involving averaging and order-of-magnitude

estimates to obtain the following one-dimensional equation for average sample-ion concentration:

$$\frac{\partial \overline{C}^1_{S,j}}{\partial t} + \langle u \rangle^0 \frac{\partial \overline{C}^1_{S,j}}{\partial x} = z_{S,j} \nu_{S,j} F \left[\frac{\partial}{\partial x} \left(\overline{C}^1_{S,j} \frac{\partial \overline{\phi}^0}{\partial x} \right) \right] + D_{S,j} \left(\frac{\partial^2 \overline{C}^1_{S,j}}{\partial x^2} \right) + \frac{8d^2 g(x,t)}{105 D_{S,j}} \left(\frac{\partial}{\partial x} \left(g(x,t) \frac{\partial \overline{C}^1_{S,j}}{\partial x} \right) \right). \quad (4.38)$$

Together equations (4.28), (4.29), (4.36), and (4.38) now form a new simplified set of governing equations for the unsteady area-averaged concentration field of all three ions, and their coupling to the potential and the velocity field in an FASS process. As described in the next subsection, a dimensionless form of this set of equations is helpful in identifying the key dimensionless parameters of the problem.

4.2.5. *Dimensionless equations*

The variables are made dimensionless as follows:

$$\underline{t} = \frac{t E_o F \nu_o}{s_S}, \quad \underline{g} = \frac{g}{-\varepsilon_o \varepsilon_r E_o \zeta_o / \mu}, \quad \underline{x} = \frac{x}{s_S}, \quad \underline{C} = \frac{C}{C_{Ao}}, \quad \underline{D} = \frac{D}{D_o}, \quad \underline{E} = \frac{E}{E_o}, \quad E_o = \frac{\phi_o}{2L}.$$

where ν_o, ζ_o, and D_o are respectively the characteristic scales for electrophoretic mobility, zeta potential, and diffusivity, and an underline denotes a dimensionless quantity. The dimensionless equations are then

$$\frac{\partial \overline{\underline{C}}^0_A}{\partial \underline{t}} + \alpha \langle \underline{u} \rangle^0 \frac{\partial \overline{\underline{C}}^0_A}{\partial \underline{x}} = \underline{D} \frac{\partial^2 \overline{\underline{C}}^0_A}{\partial \underline{x}^2} \frac{1}{Pe} + \alpha^2 \beta^2 Pe \frac{8 \underline{g}(x,t)}{105 \underline{D}} \frac{\partial}{\partial \underline{x}} \left(\underline{g}(x,t) \frac{\partial \overline{\underline{C}}^0_A}{\partial \underline{x}} \right), \quad (4.39)$$

$$- \frac{\partial \left(\overline{\underline{C}}^0_A \overline{\underline{E}}^0 \right)}{\partial \underline{x}} + \frac{(\underline{D}_A - \underline{D}_B)}{Pe(z_A \underline{\nu}_A - z_B \underline{\nu}_B)} \frac{\partial^2 \overline{\underline{C}}^0_A}{\partial \underline{x}^2} = 0, \quad (4.40)$$

$$\frac{\partial \overline{\underline{C}}^1_{S,j}}{\partial \underline{t}} + \alpha \langle \underline{u} \rangle^0 \frac{\partial \overline{\underline{C}}^1_{S,j}}{\partial \underline{x}} = \underline{D}_{S_j} \frac{\partial^2 \overline{\underline{C}}^1_{S,j}}{\partial \underline{x}^2} \frac{1}{Pe} + \alpha^2 \beta^2 Pe \frac{8 \underline{g}(\underline{x}, \underline{t})}{105 \underline{D}_{S,j}} \frac{\partial}{\partial x} \left(\underline{g}(\underline{x}, \underline{t}) \frac{\partial \overline{\underline{C}}^1_{S,j}}{\partial \underline{x}} \right) - z_{S,j} \nu_{S,j} \frac{\partial \left(\overline{C}^1_{S,j} \overline{E}^0 \right)}{\partial x}. \quad (4.41)$$

where the underlines have been removed for clarity of presentation. The initial conditions in terms of dimensionless quantities are

$$\left. \begin{aligned} &\overline{\underline{C}}^0_A(\underline{x}, \underline{t} = 0) = 0.5((1+\gamma) + (1-\gamma)\,\mathrm{erf}(\underline{x}/\delta)), \\ &\overline{\underline{C}}^1_{S,j}(\underline{x}, \underline{t} = 0) = 0.5(1 + \mathrm{erf}(\underline{x})), \end{aligned} \right\} \quad (4.42)$$

and the boundary conditions are

$$\left. \begin{aligned} &\overline{\underline{C}}^0_A(\underline{x} = -\underline{L}, \underline{t}) = \gamma; \overline{\underline{C}}^0_A(\underline{x} = \underline{L}, \underline{t}) = 1, \\ &\overline{\underline{C}}^1_{S,j}(\underline{x} = -\underline{L}, \underline{t}) = 0; \overline{\underline{C}}^1_{S,j}(\underline{x} = \underline{L}, \underline{t}) = 1, \\ &\overline{\underline{\phi}}^0(\underline{x} = -\underline{L}, \underline{t}) = 2\underline{L}; \overline{\underline{\phi}}^0(\underline{x} = \underline{L}, \underline{t}) = 0. \end{aligned} \right\} \quad (4.43)$$

The parameters governing this system of equations are

$$Pe = \frac{E_o \nu_o F s}{D_o}; \quad \alpha = \frac{-\varepsilon_o \varepsilon_r \zeta_o / \mu}{F \nu_0} = \frac{\nu_{EOF}}{\nu_{EP}}; \quad \beta = \frac{d}{s_S}; \quad \delta = \frac{s_B}{s_S}. \quad (4.44)$$

Pe is the electric Péclet number, expressed as the ratio of diffusion time to electromigration time; α is the ratio of electro-osmosis to electrophoretic mobility; β is the ratio of channel width to characteristic length scale for the initial sample-ion concentration distribution; and δ is the ratio of the length scale of the initial BGE- and sample-ion concentration gradients. As we shall see, once the geometry of the system is fixed and s_s is minimized by an efficient sample injection scheme, the parameters controlling the rate of stacking and the achievable concentration increase are Pe, α, and γ. Also, minimally dispersive conditions are associated with low values of α (i.e. suppressed EOF conditions).

5. Method of solution

The first step in the solution is to solve for the velocity field using the initial conditions, equation (4.42). Second, the buffer-ion equation (4.39) is solved numerically using a parabolic PDE solver in Matlab (The Mathworks, Inc., Natick, MA). Once the buffer-ion concentration distribution is known, the electric field distribution is calculated by solving equation (4.40) analytically:

$$\overline{\underline{E}}^0(\underline{x},\underline{t}) = \frac{\underline{Q}}{Pe\overline{\underline{C}}_A^o}\frac{\partial\overline{\underline{C}}_A^0}{\partial\underline{x}} + \frac{2\underline{L} + (\underline{Q}/Pe)\ln\gamma}{\overline{\underline{C}}_A^0\displaystyle\int_{-\underline{L}}^{\underline{L}}\frac{\mathrm{d}\underline{x}}{\overline{\underline{C}}_A^0}}. \tag{5.1}$$

The resulting electric field distribution is then substituted into the sample-ion equation (4.41) and the sample-ion distribution is computed using the aforementioned PDE solver.

We have further reduced the (already short) computational time associated with our solution method by leveraging a simplification suggested by the large value of $L/s_S = O(1000)$. Namely, the axial integrals in equations (4.14) and (4.15) are calculated analytically by neglecting the contributions from the narrow region where the gradients in concentration occur.

6. Dispersion model results

The modelling results for the cross-section-averaged background-ion A concentration, electric field, and sample-ion, C, concentration distribution are described in figure 7(*a–c*). Figure 7(*a*) shows how both molecular diffusion and convective dispersion disperse the boundary between the high- and low-concentration regions of the background electrolyte ion A. Because ions A and B are present in concentrations much higher than the sample ion C, the development of these ions is approximately the same as the development of two neutral species subject to non-uniform electro-osmotic flow in the channel and an effective diffusivity. As shown in equation (4.3), the zeroth-order solution is exactly this type of convective diffusion process. That is, since background electrolyte ions follow binary electrolyte dynamics, there is no electromigrational contribution to the concentration distribution. The background electrolyte establishes the conductivity field which in turn establishes the electric field distribution (figure 7*b*). Figures 7(*a*) and 7(*b*) also show the translation of the inflection point in the A concentration profile in the direction of the electro-osmotic flow. This front translates at a rate equal to the bulk velocity of the system, U_{bulk} (related to the axial integral of the slip velocity through equation (4.15)).

Figure 7(*c*) shows the development of the sample-ion concentration (species C). The sample ions react passively (and instantaneously) to the background electric

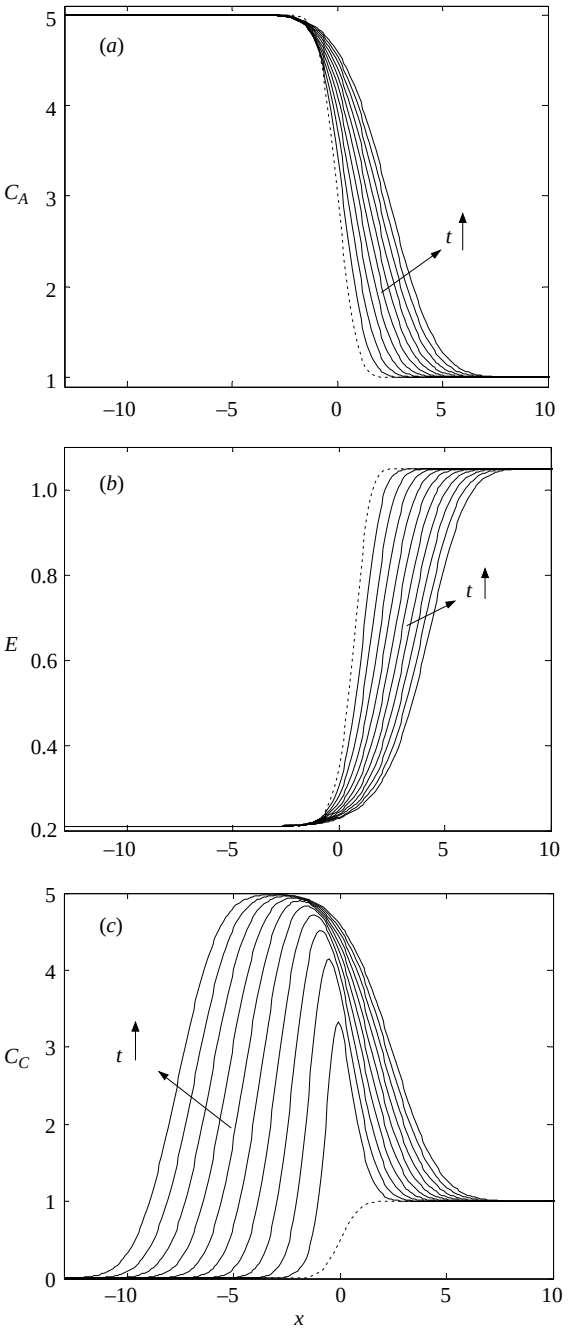

FIGURE 7. Predicted evolution of the (*a*) background electrolyte-ion concentration, (*b*) electric field, and (*c*) sample-ion concentration field. The dotted curves refer to the initial condition. The dispersion model parameters for these plot are $Pe = 60$, $\alpha = 0.05$, $\gamma = 5$, $\beta = 2$, and $\delta = 1$. In all cases, multiple curves are shown for times separated by 100 ms.

and velocity fields as determined by the convective-diffusion of the background electrolyte ions. Electrophoretic flux of the anionic sample species from the region of low conductivity (high field) to high conductivity (low field) results in a local

accumulation leading to increased concentration. As expected given our assumptions, the maximum concentration enhancement factor is equal to γ.

We can validate our numerical scheme and the perturbation model by analysing the high-*Pe* limit of the regular perturbation model (equations (4.39)–(4.41)) in the absence of EOF and comparing it to the analytical solution for a nonlinear, hyperbolic electromigration process (equation (3.7) solved using the method of characteristics, MOC). Since the analytical MOC model is valid for the constant current density case, we solve the dispersion model for the same condition. This comparison between the dispersive and non-dispersive model is shown in figure 8. First, figure 8(*a*) shows that there is excellent agreement between the two approaches in the limit of zero EOF and infinite *Pe*. This shows that for small enough values of the parameter ε, the first-order equation (4.41) is sufficient to accurately predict the spatial and temporal distribution of the sample-ion concentration.

The regime of applicability of the nonlinear MOC solution can be explored by systematic variation of Pe and α. These results are shown in figures 8(*b*) and 8(*c*) for the quantity of most interest: the temporal evolution of the peak concentration of the sample ion. Figure 8(*b*) shows the case of zero EOF where only *Pe* is varied by changing the applied current density, j_o. For *Pe* values of 200 and above, the MOC solution agrees with the more general dispersion model to within 5 %. Diffusion processes become critical for lower values of *Pe*. The case where *Pe* is sufficiently large but where advective dispersion is important is explored in figure 8(*c*). Here we use a value of $Pe = 210$ for the dispersion model but vary the value of α between 0 and 0.3. The comparison shows that the MOC solution is accurate to within 10 % in the high-*Pe* limit for values of α below 0.1. Higher values of α result in significant contributions of advective dispersion and the MOC solution is again limited. Lastly, figure 8(*c*) shows that for a typical range of ε, between 0.01 and 0.001, the MOC solution is a weak function of ε. This again confirms that for small values of ε, the dynamics of the background electrolyte is decoupled from the sample-ion distribution and the first-order perturbation solution is a good approximation.

In the presence of EOF, the overall drift of anionic sample ions is determined by the competing effects of EOF (in the direction of the electric field for negative zeta potentials) and electromigration (in the opposite direction). This competitive nature of the transport results in the peak migration behaviour shown in figure 9. In this figure, we plot the location of the stacked analyte peak (the location of $C_{c,max}$) as a function of time for various values of the EOF mobility parameter α. In the absence of EOF ($\alpha = 0$), electromigration leads to a drift of the negatively charged sample ions in a direction opposite to the electric field. In the case of dominant EOF ($\alpha = 0.5$), the sample peak is convected in the direction of electric field. In an intermediate parameter range (near $\alpha = 0.14$), the peak position trace shows an inflection point. Initially the motion of the peak is dominated by electromigration and then, as the conductivity gradient diffuses, EOF advective flux dominates and the peak migrates in the direction of the electric field.

Next, we consider the effects of diffusive and advective dispersion on concentration increase as a function of γ for a given duration of stacking. We choose the constraint of fixed analysis time as we are interested in FASS as a preconcentration step prior to electrophoretic separation. These fixed-time comparisons help to determine the time needed to achieve adequate concentration enhancement and the initial condition of the subsequent uniform-conductivity separation process. Figure 10 shows clearly that there is an optimum value of γ for a given set of parameters and analysis time. This result is in contrast to the ideal dynamics presented before, which showed that

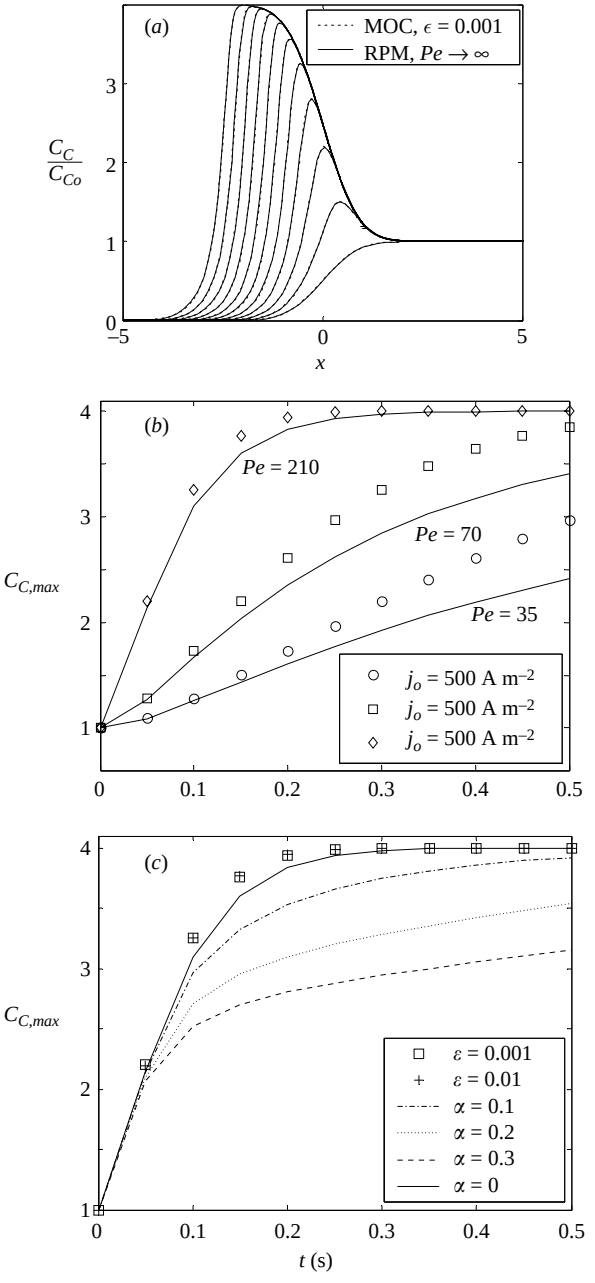

FIGURE 8. Comparison of the method of characteristiscs (MOC) solution and the regular perturbation method (RPM) solution for the sample-ion concentration profiles. (*a*) The spatial development of sample concentration. The applied current density is $1500\,\mathrm{A\,m^{-2}}$ and $\gamma = 4$. (*b*) Effect of current density on the peak concentration versus time. The mobility values used in this simulation are listed in table 1. The perturbation model results are shown as solid lines. For the perturbation model calculations: $\alpha = 0$, $\beta = 1$, and $\delta = 1$. (*c*) Effect of the EOF parameter α on the peak concentration versus time. MOC results are shown using symbols and the dispersion model results are represented by lines. The applied current density here is $3000\,\mathrm{A\,m^{-2}}$, which corresponds to $Pe = 210$. For the dispersion model calculations: $\beta = 1$ and $\delta = 1$.

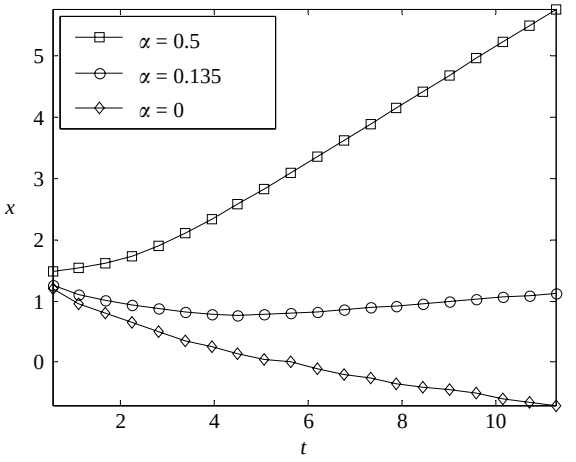

FIGURE 9. Axial location of the sample-ion peak as a function of time for three different EOF mobilities. The parameters for the model are $Pe = 167$, $\gamma = 9$, $\beta = 0.7$, and $\delta = 1.27$. At intermediate values of α (near $\alpha = 0.14$) the location of the peak concentration first moves against the electric field and then in the direction of the electric field.

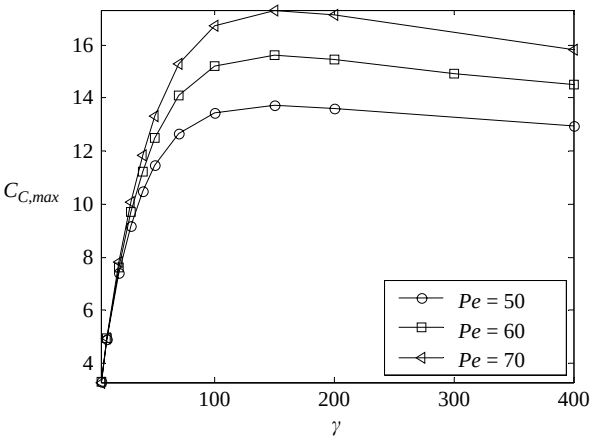

FIGURE 10. Optimum value of γ for fixed stacking times of 1 s. The parameters for the dispersion model are: $\alpha = 0.5$, $\beta = 2$, and $\delta = 1$. For a given analysis time and fixed values of Pe, α, β, and δ, there is a unique value of γ that provides maximum concentration enhancement.

increasing γ always increases the concentration enhancement (figure 5). This is an important feature of the model as it gives experimentalists a method of choosing values of γ to yield optimal signal detections.

The existence of an optimal value of γ can be better understood by considering the scaling of the parameters of interest. Equations (3.12) and (3.14) (and figure 2) show that the maximum sample concentration is proportional to γ:

$$C_{C,\max} \propto \gamma. \tag{6.1}$$

In contrast, from equations (2.4) and (2.5), the ratio of the EOF velocity in the

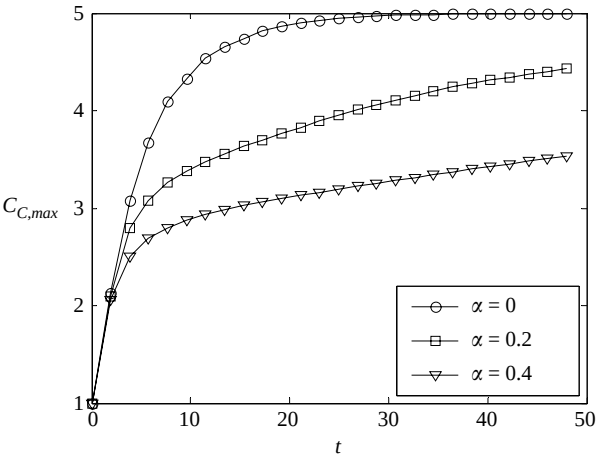

FIGURE 11. Effect of EOF mobility parameter α on the rate of concentration increase. The model parameters here are $Pe = 60$, $\gamma = 5$, $\beta = 2$, and $\delta = 1$. The net concentration enhancement time was fixed at 1 s.

low-conductivity region to the value in the high-conductivity region scales as

$$\frac{U_{EOF,S}}{U_{EOF,B}} \sim \frac{\varsigma_S E_S}{\varsigma_B E_B} \sim \gamma^{1.2} \tag{6.2}$$

so that the advective dispersion effects of mismatched slip velocities is negligible for low γ but then dominates at high γ. A similar scaling observation has also been made by Burgi & Chien (1991) who discuss the existence of an optimum γ using simple scaling arguments. They developed an algebraic model for the long-time behaviour of a finite-length sample plug variance as a function of γ sing a one-dimensional Taylor dispersion approximation. In contrast to their model, the dynamic model described here allows quantitative prediction of both temporal and spatial development of the sample ion, background electrolyte ions, and electric field profiles.

Another important parameter determining the convective dispersion and hence rate of concentration increase in FASS is α, or the ratio of electro-osmotic and electrophoretic mobilities. For a typical value of electrophoretic mobility (e.g. 3×10^{-13} m mol N^{-1} s^{-1}), α is approximately equal to 2 for glass microchips. Therefore, the dispersion dynamics of untreated glass chips are well in the advection regime. However, at least an order of magnitude reduction in electro-osmotic mobility is possible by adding dynamic surface coatings using neutral water-soluble polymers (Preisler & Yeung 1996). It is therefore interesting to experimentalists to quantify the importance of suppressing EOF in determining maximum achievable concentration increases. In figure 11 we consider the effect of α on the rate of concentration increase. At short times, the rate of concentration increase is independent of α. The increase in width of the area-averaged conductivity gradient region due to dispersive effects is, at short times, negligible and so the dynamics is governed by initial conditions. This short time can be defined as

$$t \ll \frac{s_S^2}{D_{eff}} \tag{6.3}$$

where D_{eff} is a characteristic scale for the dispersive effects. After this initial development time, the rate of concentration increase is increasingly governed by

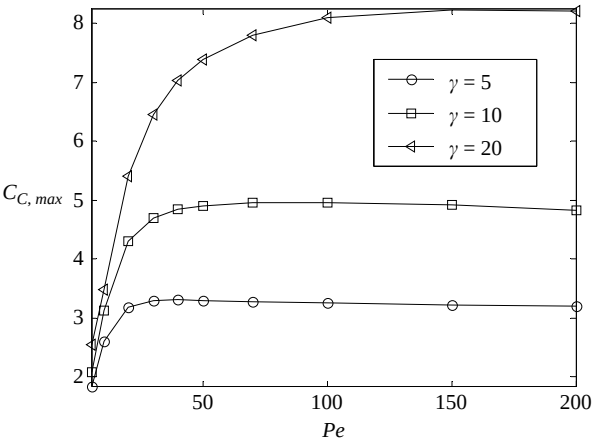

FIGURE 12. Optimum value of *Pe* for a fixed stacking time of 1 s. The parameters for the dispersion model are $\alpha = 0.5$, $\beta = 2$, and $\delta = 1$. At low *Pe*, diffusive dispersion dominates and concentration enhancement suffers. At high *Pe*, advective dispersion is dominant and again concentration enhancement suffers. For fixed γ and analysis time, there is a unique, optimal *Pe* (e.g. an optimal electric field for a given channel system) which results in maximum concentration increase.

dispersive effects and various rates of growth are apparent for different values of α. Note that, even for the case of a ten-fold decrease in electro-osmotic mobility ($\alpha = 0.2$), there is significant convective dispersion. This result has important consequences for the design of microchip-based FASS systems because a slower rate of concentration increase can adversely affect the amount of sample required per separation as well as the throughput of the device. To increase the rate of concentration enhancement, the electric field and thus Péclet number should be increased. Figure 12 describes the effect of *Pe* on maximum concentration achievable for a given analysis time. Initially, increases in *Pe* are favourable for concentration enhancement. This is due to a reduced contribution of molecular diffusion which scales as Pe^{-1}. However, as *Pe* is increased further the concentration increase slows down and, past a critical *Pe*, the achievable concentration begins to decrease. The latter effect is due to the fact that convective dispersion increases with increasing *Pe*. Equations (4.39) and (4.41) show that the dispersion term scales as $\alpha^2\beta^2 Pe$. There is therefore an optimum value of *Pe* for a given analysis time and fixed values of γ, α, and β. Note that, in practice, the optimum value of *Pe* may be somewhat smaller than that predicted by our dispersion model since we do not account for the effects of Joule heating (Grushka, McCormick & Kirkland 1989). Joule heating is proportional to the square of the local electric field and is expected to be important for very high field strengths and relatively large channels.

Lastly, in figure 13 we consider sample stacking and separation dynamics of three sample ions. The initial sample concentration profile is described by

$$\underline{C}_{S,j}(\underline{x}, \underline{t} = 0) = \frac{\varepsilon}{2}(\mathrm{erf}(\underline{x}) - \mathrm{erf}(\underline{x} - 2\underline{h})) \tag{6.4}$$

where $\underline{h}$ is the dimensionless width of the sample plug. The buffer-ion initial concentration is described by equation (2.7). Such a sample–buffer configuration was used by Jung *et al.* (2003) to demonstrate 1000-fold signal increase using FASS. Figure 6 shows that initially there is rapid stacking (accumulation) of the sample ions

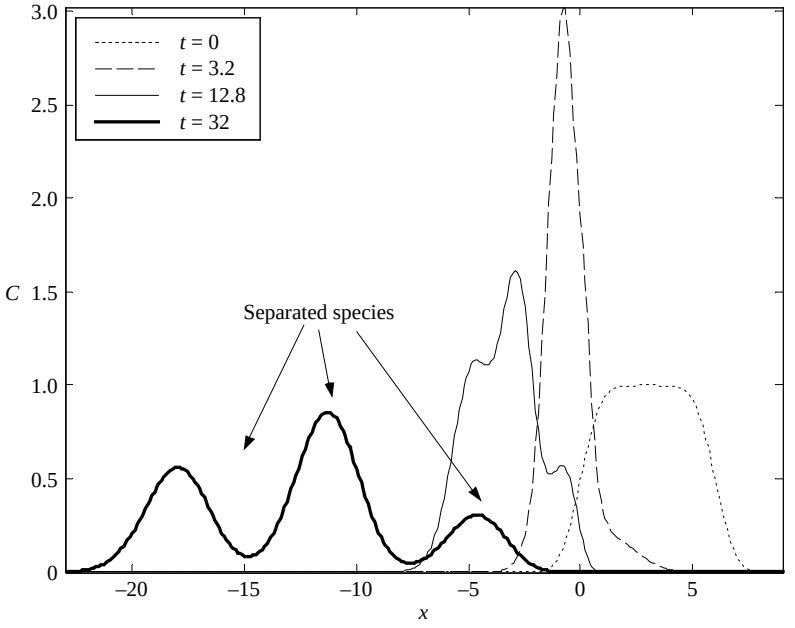

FIGURE 13. Stacking and separation dynamics of three negatively charged sample species. The model parameters are $Pe = 40$, $\gamma = 5$, $\beta = 2$, $\alpha = 0.05$, $\delta = 1$, and $h = 6$. The dimensionless electrophoretic mobilities of the species are 1, 2, and 3, respectively. The initial dimensionless concentrations of the sample species are 1/6, 1/2, and 1/3, respectively.

as they exit the low-conductivity region and enter the high-conductivity region. Once sample ions enter the high-conductivity region, sample stacking ends and ions are subsequently electrophoretically separated into three distinct peaks. The dispersion model can be used to optimally design FASS-based electrophoretic separation systems for analysis of multiple sample species. For example, the model predictions can guide the location of the detector and width of initial sample plug to ensure adequate signal-to-noise ratio and resolution.

7. Experimental results and model validation

An inverted epifluorescence microscope (Olympus IX70) equipped with a 10X objective (Olympus, NA = 0.4) was used for imaging the concentration fields of sodium fluorescein dye solutions. Illumination from a mercury lamp was spectrally filtered at the peak fluorescein absorption and emission wavelengths of 485 nm and 535 nm, respectively. Images were captured using a frame transfer intensified CCD camera (I-PentaMAX, Gen III, Princeton Instruments) with a 512×512 CCD pixel array and 12-bit digitization. Up to 58 frames per second were obtained by imaging only a 101×512 pixel sub-section of the CCD array. The exposure time was set to 10 ms. A low-fluorescence Borofloat glass microchip (Micralyne, Alberta, Canada) with a staggered-T channel geometry was used for all experiments. The microchannel width is 50 μm and the centreline depth of the channels is 20 μm. The channels have the characteristic shape of an isotropic wet etch. The length of the vertical channel is 8 mm and the length of the horizontal channel is 85 mm. The length of the injection region (the centre-to-centre distance between the two staggered T sections) of this chip is 100 μm. A high-voltage power supply (Micralyne, Alberta, Canada, 6 KV maximum)

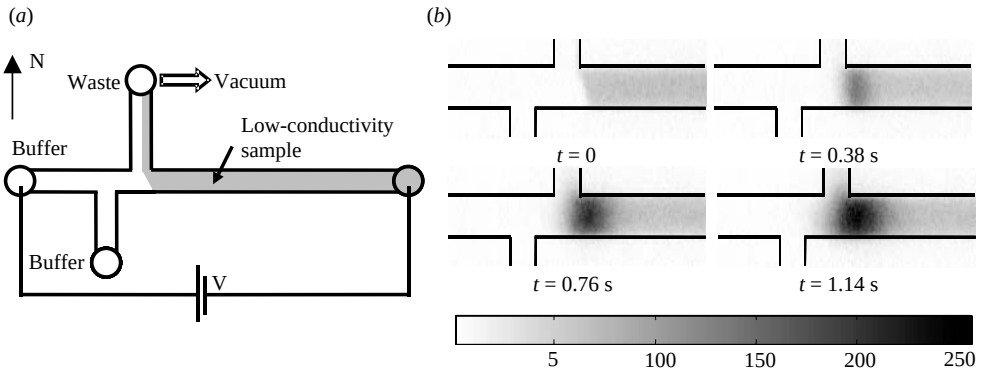

FIGURE 14. (*a*) Schematic of microchip for single interface stacking experiments. Width and centreline depth of channels were 50 and 20 microns, respectively. (*b*) Epifluorescence CCD images showing establishment of initial condition for conductivity gradient and subsequent stacking across the interface. The sample was anionic 17 μM bodipy dye and the buffer was HEPES at pH = 7.

was used to control platinum electrode potentials mated to the chip reservoirs. In the stacking experiments, we used a 78 mM HEPES buffer prepared by titrating HEPES acid against sodium hydroxide to obtain a pH of 7.2. The solution's electrical conductivity was measured at $0.19\,\mathrm{S\,m^{-1}}$. The low-conductivity sample solution was prepared by diluting the stock-buffer solution with distilled water. The sample was 17 μM bodipy dye (Molecular Probes) dissolved in diluted buffer. The microchip was flushed with acidified poly(ethylene oxide) solution to suppress EOF. This acidified PEO treatment is described by Preisler & Yeung (1996). We used a 0.4 % (w/v) solution of PEO and filled the chip several hours before experiments in order to establish a uniform coating. After this surface treatment step, the microchip was flushed with the HEPES buffer for 5 min at a flow rate of $20\,\mu\mathrm{L\,h^{-1}}$ to remove PEO solution.

CCD images of the fluorophore in the channels were corrected by applying the following matrix operation to each image:

$$I_{corr} = \frac{I_{raw} - I_{background}}{I_{flatfield} - I_{background}}. \tag{7.1}$$

In this approach for quantitative imaging, a background image is subtracted from the raw image and this difference is normalized by the difference between a flatfield and the background image. The flatfield image was obtained by imaging the microchannel filled with a homogenous concentration of dye. To compare the two-dimensional image data with the area-averaged model, the intensity data for the pixel regions of the microchannel images were averaged along the vertical direction (i.e. the width of the microchannel) to form one-dimensional, cross-section-area-averaged axial intensity profiles.

The interface between high- and low-conductivity buffer regions is generated by applying a vacuum at the north reservoir as shown in figure 14(*a*). Once a buffer–buffer interface is established, the vacuum is released and an axial electric field is applied. Upon application of an axial electric field along the west-to-east direction, sample stacks at the interface between buffer streams. Figure 14(*b*) shows images of the stacking process at selected times. In figure 15, instantaneous images of the stacking process are shown for a case where EOF was not suppressed. Since the EOF

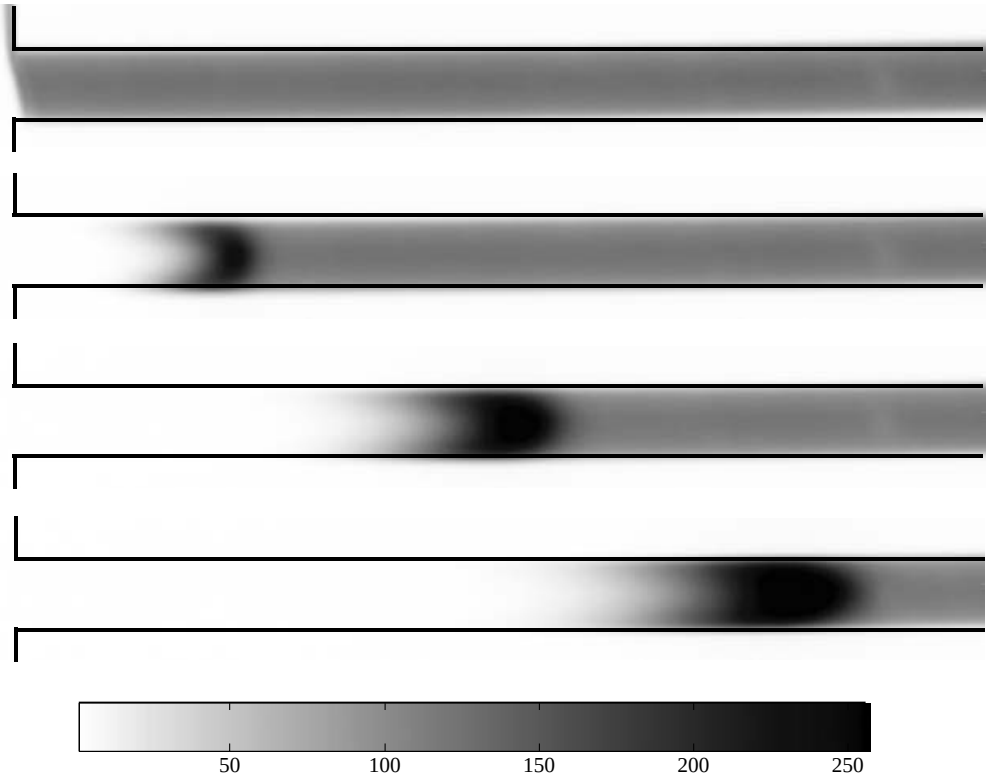

FIGURE 15. CCD images of FASS in an untreated channel with significant EOF mobility. The images clearly show the development of stacked fluorescein in the favourable-pressure-gradient region (i.e. the high-conductivity region). The sample was 25 μM fluorescein dye dissolved in 5 mM Borate buffer. The background electrolyte for this particular experiment was 25 mM Borate buffer (pH = 9.2). The electric field in the sample region was 50 V cm^{-1} and $\gamma = 4$.

velocity in all regions is greater than the negative electrophoretic velocity of fluorescein dye, the stacked region moves in the direction of EOF. The images clearly show the favourable-pressure-gradient-induced curvature of the stacked ions on the downstream (left-hand) side of the interface. As described earlier, these pressure gradients act to disperse sample and reduce the efficiency of FASS. From figure 14(*b*) and figure 15 the efficacy of the EOF-suppression method is apparent as the conductivity interface is nearly stationary and there is negligible pressure-induced curvature of stacked analyte. Figure 16 shows the temporal development of the spatial concentration distribution of sample ions. To improve signal-to-noise ratio, the intensity profiles were convolved with a Gaussian filter. The width of the filter was chosen to be 5 % of the half-width half-maximum of each of the profiles at each time step. The dynamics of the peak concentration of these data is shown in figure 17(a, b) for various values of the electric field in the low-conductivity region, E_S, of the channel. Since the length of the interface region is small compared to the length of the channel, E_S is related to the applied potential along the channel as follows:

$$E_S = \frac{\gamma V}{L_T(1 + (\gamma - 1)a)} \tag{7.2}$$

where V is the applied voltage, L_T is the channel length and a is the fraction of

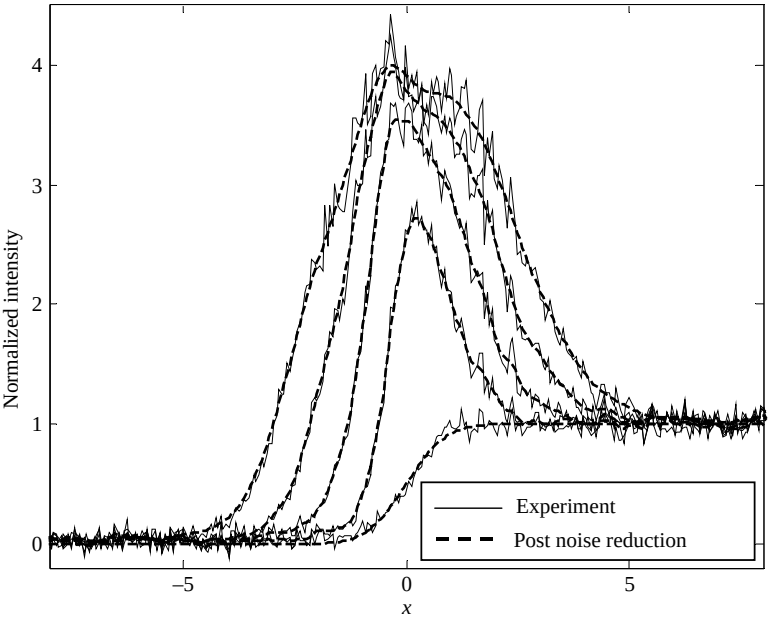

FIGURE 16. Measured axial intensity profiles for sample ions. The profiles were obtained by averaging two-dimensional image intensity data along the width of the channel. The applied nominal electric field (potential difference divided by channel length) was $588\,\mathrm{V\,cm^{-1}}$ and $\gamma = 4$. Time between individual profiles is 0.15 s. To reduce image noise, the raw data was low-pass filtered using a Gaussian kernel with a standard deviation width equal to 5 % of the half-width of each peak at the half-maximum intensity level (HWHM) at each time step (both raw data and filtered data are shown above). The sample ions develop as a travelling wave with peak height increasing in time until the concentration enhancement reaches a maximum value of γ. Due to the nature of the initial sample concentration distribution, the variance of the stacked sample increases indefinitely with time.

the channel occupied by the low-conductivity sample. As predicted by the dispersion model, the peak intensity increases roughly exponentially at first and then saturates at a maximum achievable concentration enhancement of γ. The rate of concentration enhancement increases with electric field. For the same electric field, higher γ conditions require a longer time to achieve maximum concentration enhancement. Qualitatively this behaviour agrees with the characteristic time scale derived in equation (3.15) for ideal stacking dynamics.

To quantitatively compare our model predictions with experimental data, we model the buffer solution as composed primarily of two ions: a sodium cation and a HEPES. This is appropriate since these ions are the dominant species in the electrolyte solution and hence govern the conductivity gradient. Typical values of various physical parameters including the mobilities of sample and buffer ions are listed in table 1. The mobility of bodipy dye was estimated from the results of Bharadwaj *et al.* (2002). The mobility of the HEPES anion was estimated from conductivity measurements (using the known mobility of the sodium ion). The diffusion coefficients for the buffer ions were estimated from mobility values using the Nernst–Einstein equation,

$$D_i = RT\nu_i. \tag{7.3}$$

Parameter s_S, the characteristic length scale of the initial sample-ion distribution, was obtained from fluorescence imaging measurements of the initial sample-ion intensity

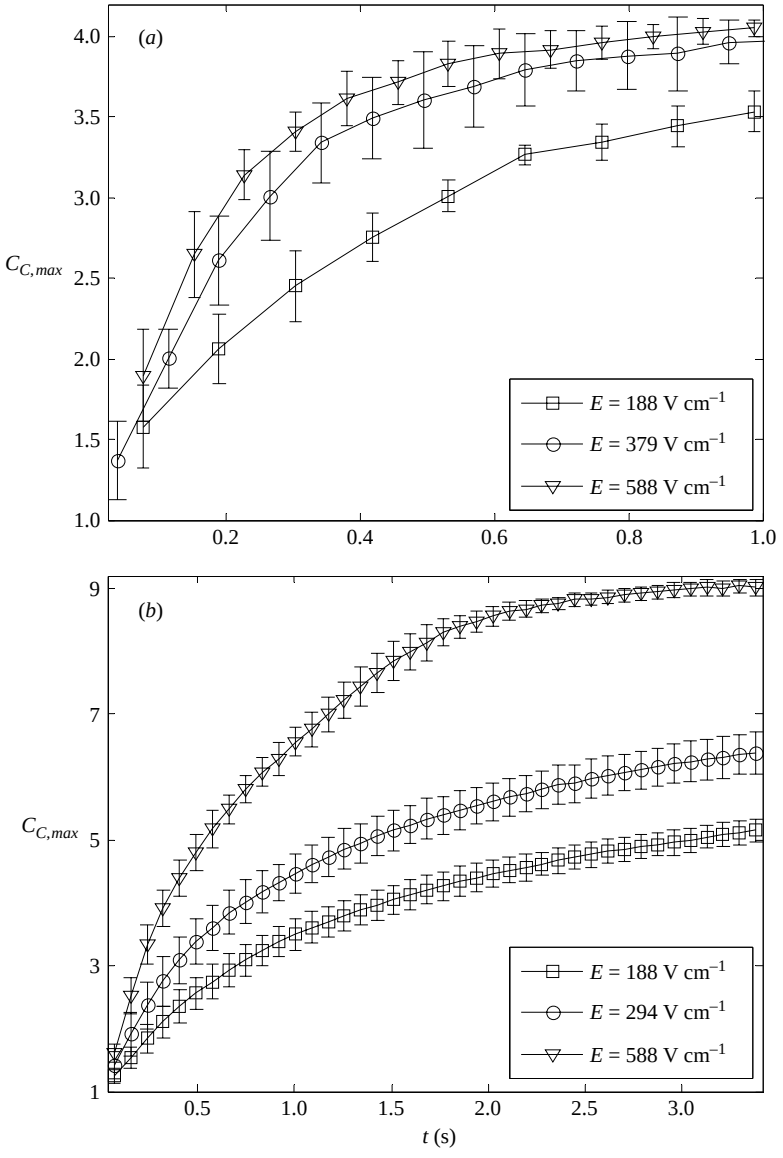

FIGURE 17. Measured peak concentration versus time for three electric field values. Cases shown are: (*a*) $\gamma = 4$ and (*b*) $\gamma = 9$. The data represent an average of four to six realizations for each field strength and γ.

profile. The characteristic length scale of the initial buffer-ion concentration gradient, s_B, can be estimated from that of the sample ion as follows:

$$s_B = s_S \sqrt{\frac{\overline{D}}{D_C}}. \tag{7.4}$$

The only remaining unknown parameter is the electro-osmotic mobility of the channel walls, and hence the parameter α. The electro-osmotic mobility of the polymer-coated channel walls is non-uniform and unsteady due to the developing

Symbol	Description	Value
ν^{+}_{Na}	Sodium ion electrophoretic mobility	5.2×10^{-13} m mol N^{-1} s^{-1}
ν^{-1}_{HEPES}	HEPES ion electrophoretic mobility	2.4×10^{-13} m mol N^{-1} s^{-1}
ν^{-1}_{Bodipy}	Bodipy electrophoretic mobility	2×10^{-13} m mol N^{-1} s^{-1}
ν_{EOF}	EOF mobility	$5 \times 10^{-14} - 5 \times 10^{-13}$ m mol N^{-1} s^{-1}
d	Channel half-depth	10 μm
w	Channel half-width	25 μm
s_S	Characteristic length scale of the initial sample-ion distribution	5–40 μm
E_o	Applied electric field	200–600 V cm^{-1}

TABLE 1. Parameters and characteristic values.

concentration gradients in the channel, and experimental measurement of the local, instantaneous electro-osmotic mobility field in this flow is difficult. We therefore used the absolute value of the axial-average electro-osmotic mobility as a free parameter in comparing our model results to experimental results. This value was obtained from the measurement of the peak location versus time data. Note that this fitting method merely registers the (slight) motion of the predicted and experimental peak locations and has a single value for each experiment.

This experimentally determined α value was then used to predict the development of the full velocity field in the channel and the dynamics of the area-averaged concentration profiles (including peak concentration values). Figure 18(*a–c*) shows comparisons between model predictions and experimentally measured concentration profiles. Experiments are shown for $\gamma = 4$ and 9 and E_S values of 379 and 588 V cm^{-1}. There is very good quantitative agreement between measured area-averaged concentration profiles and the model prediction throughout the time of observation. Note that, as shown in figure 14(*b*), for times approaching 1 s the region of high area-averaged concentration becomes two-dimensional as it enters the staggered-T injection region of the system (which cannot be captured by our model). The experimentally determined axial-averaged mobility value for the experiments shown in figure 18 are 0.5×10^{-14}, 0.5×10^{-14}, and 0.3×10^{-14} m mol N^{-1} s^{-1}, respectively. These values are within the range of expected values for PEO-treated glass channels with a buffer pH of 7 (Preisler & Yeung 1996). The model is able to capture important features such as the development of peak width and the temporal growth of the maximum concentration.

Figure 19 shows a more detailed comparison of model predictions for the temporal development of the peak concentration and experimental data for three electric fields and two γ values. The error bars in these figures represent 95 % confidence intervals obtained from four to six realizations, and are therefore a measure of the high degree of repeatability of the experiment. The model captures the correct trends for variations in both γ and electric field. The model predicts maximum concentration values within 10 % of experiments for all times for the $\gamma = 4$ case. For $\gamma = 9$, and electric fields below 300 V cm^{-1}, the model predicts maximum concentration values within 20 % of the experimental data. However, at $\gamma = 9$ and an electric field of 588 V cm^{-1}, the model slightly overpredicts the magnitude of the peak concentration. This discrepancy is probably due to expected limitations of the model at high values

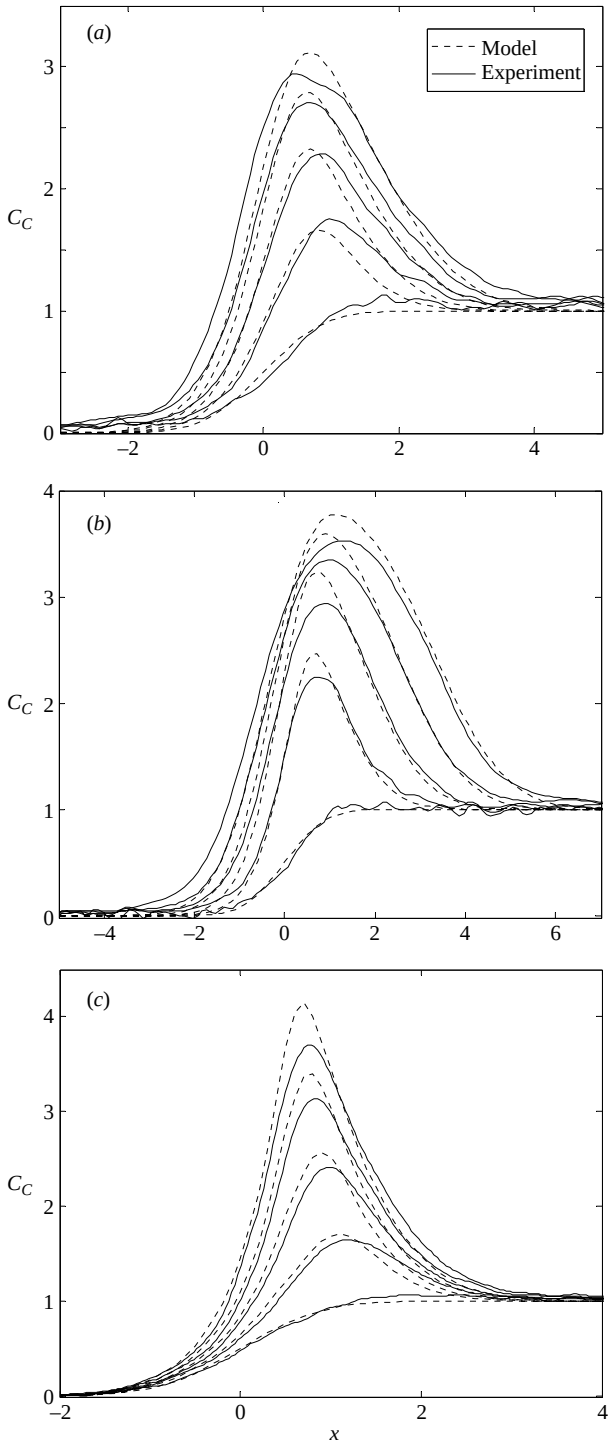

FIGURE 18. Comparison of model prections and measured concentration profiles. In (*a*), $\gamma = 4$, $E_o = 379\,\mathrm{V\,cm^{-1}}$, and time between frames was 76 ms. The model parameters are $Pe = 55$, $\alpha = 0.23$, $\beta = 0.28$, $\delta = 1.27$. In (*b*), $\gamma = 4$, $E_o = 588\,\mathrm{V\,cm^{-1}}$, time between frames was 76 ms. The model parameters were $Pe = 59$, $\alpha = 0.23$, $\beta = 0.4$, $\delta = 1.27$. In (c), $\gamma = 9$, $E_o = 588\,\mathrm{V\,cm^{-1}}$, and time between frames was 68 ms. The model parameters were $Pe = 167$, $\alpha = 0.14$, $\beta = 0.14$, $\delta = 1.27$.

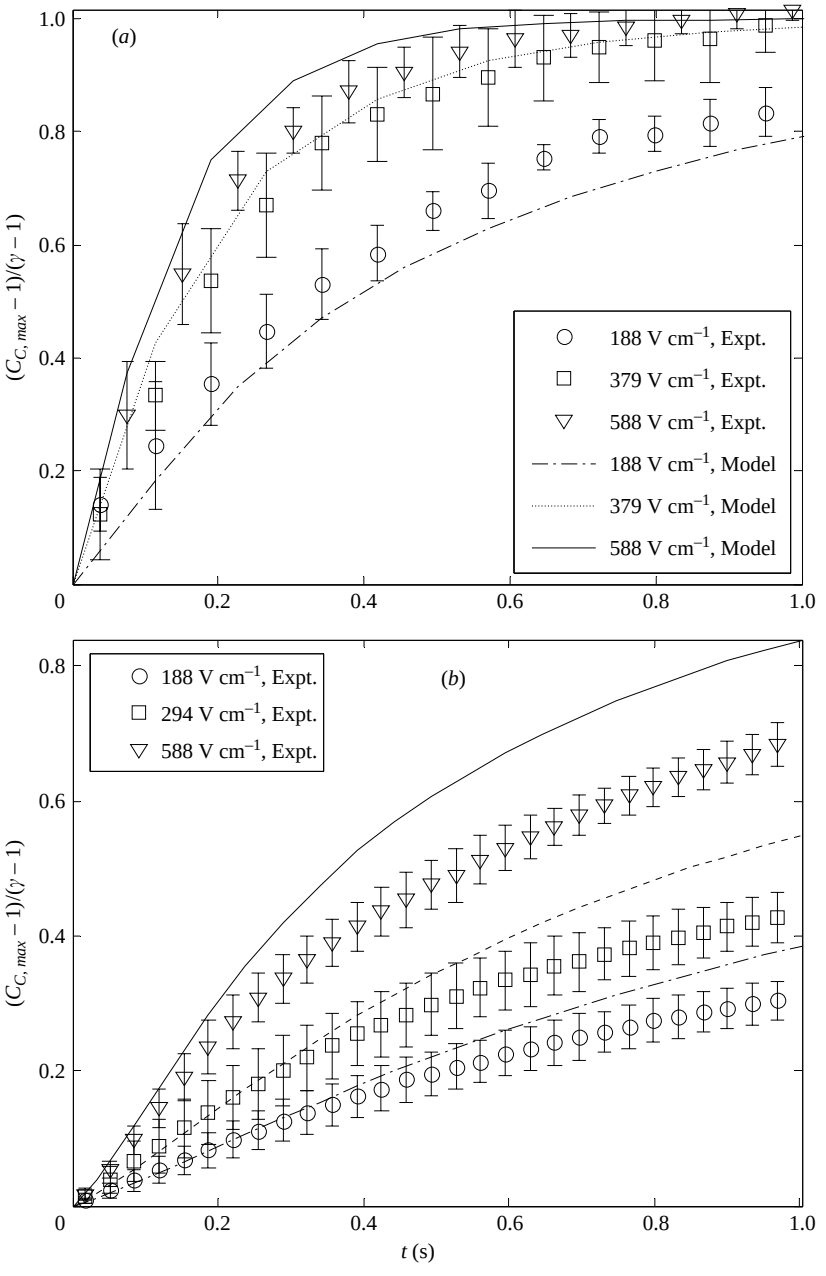

FIGURE 19. Comparison of model predictions and measured rate of increase of peak concentration value. (*a*) Model predictions and measurements for $\gamma = 4$ and three electric field values. The respective model parameters for the low, medium, and high electric fields are: $Pe = 22$, $\alpha = 0.18$, and $\beta = 0.35$; $Pe = 40$, $\alpha = 0.2$, and $\beta = 0.38$; $Pe = 82$, $\alpha = 0.22$, and $\beta = 0.28$. (*b*) Model predictions and measurements for $\gamma = 9$ and three electric field values. The dash-dot, dotted and solid lines refer to the model predictions for applied electric fields of 188, 294 and 588 V cm^{-1}, respectively. The respective model parameters for the low, medium, and high electric fields are: $Pe = 48$, $\alpha = 0.14$, and $\beta = 0.16$; $Pe = 77$, $\alpha = 0.22$ and $\beta = 0.15$; $Pe = 162$, $\alpha = 0.1$, and $\beta = 0.14$. In all the model predictions, $\delta = 1.27$.

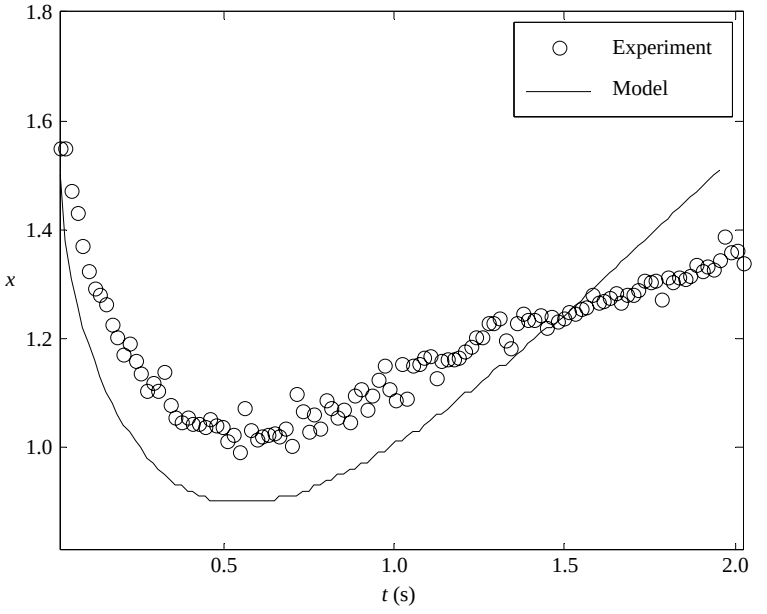

FIGURE 20. Comparison between model and experiment for peak location versus time for an intermediate α case showing an inflection point. The parameter values for the model predictions are $Pe = 78$, $\alpha = 0.15$, $\beta = 0.15$, and $\delta = 1.27$. To reduce effects of peak-locking in the peak finding algorithm (i.e. to reduce discretization errors), a five-point Gaussian function was fitted to the data in the region of the intensity peaks and the centroid of this function was tracked to obtain the peak location data.

of both γ and applied field. For example, in our model development, we assume convective–electromigration–diffusion dynamics in a purely two-dimensional flow in a wide, shallow channel (neglecting the influence of sidewalls). In reality, however, the microchannels in the experiment have a D-shape characteristic of an isotropic etch with a width to maximum depth ratio of 2.5. In future refinements of this model, it may be possible to relax this assumption by incorporating more comprehensive dispersion dynamics. For example, Dutta & Leighton (2001) have investigated the effect of isotropic-etched microchannel geometries on the dispersion coefficient for simple pressure-driven flows. Their analysis shows that the dispersion coefficients for the D-shaped channels can be three to four time larger than those predicted by simple two-dimensional analysis. Such advective–diffusion effects would be most important in our flow for large γ values (associated with larger internally generated pressure gradients) and the large Péclet numbers associated with high electric fields. Another possible refinement of this model would include dispersive effects due to joule heating (Grushka *et al.* 1989) which should also lead to reduction in the rate of concentration increase.

Lastly, figure 20 shows that the anomalous peak migration behaviour predicted by the model (see figure 9) is observed within the current experimental parameter range. At these conditions, the sample peak initially migrates in a direction opposite to that of the electric field and then reverses direction and begins migration in the direction of the electric field. As described earlier, this is a manifestation of the competing effects of electromigration of a negatively charged sample ion in a direction opposite

to the electric field and advection of the sample via residual electro-osmotic flow in the direction of electric field.

8. Conclusions

We have formulated an electromigration–diffusion–advection model to investigate FASS dynamics at an interface between high- and low-conductivity electrolyte solutions. We used a regular perturbation analysis, using the ratio of sample and background electrolyte concentration as the expansion parameter, to simplify the governing equations. The resulting equations are area-averaged to yield a one-dimensional dispersion model for FASS. The model predicts area-averaged background electrolyte concentration field, electric field, and sample-ion distribution. The model can be used to optimize the efficiency of FASS. For example, the model predicts optimum values of Pe and γ for maximum concentration enhancement, for a given analysis time. We have performed experiments to measure the unsteady concentration fields in FASS using a glass microchip. The experiments demonstrate that an acidified poly(ethylene oxide) (PEO) coating can be used to suppress EOF in a borosilicate microchip and thereby reduce advective dispersion due to EOF. Measured concentration profiles in single-interface FASS experiments show that peak concentration initially increases exponentially with time and then asymptotes to a maximum concentration enhancement factor of γ. There is very good quantitative agreement between the model predictions and the experimentally measured unsteady concentration fields. Finally, we have experimentally and theoretically observed a regime of peak migration wherein the stacking sample peak migrates first in a direction opposite to electric field and then reverses direction after a short time. This behaviour is a result of the competing effect of electromigration of negatively charged sample ions and convection due to the electro-osmotic flow.

Further improvements to the model can be made by accounting for the three-dimensional effects of typical D-shaped, wet-etched channel cross-sections. More sophisticated dispersion analyses of the unsteady three-dimensional velocity field should extend the predictive ability of the present model.

This work was sponsored by DARPA (Contract Number F30602-00-2-0609) with Dr. Anantha Krishnan as contract monitor and by an NSF PECASE Award (J. G. S., contract number NSF CTS0239080) with Dr Michael W. Plesniak as contract monitor.

Appendix

As described by Lin *et al.* (2003) and Chen *et al.* (2005), an electric field applied parallel to a conductivity gradient leads to an accumulation of net charge in the bulk liquid regions of an electrokinetic flow field, outside the electric double layer. This net charge can couple with the applied electric field in the channel and result in a body force that can introduce vorticity into the bulk flow and destabilize the flow. Combining Gauss's law and a relation for the conservation of electromigration current, this net charge can be approximated as $\rho_E \approx \varepsilon E \cdot \nabla\sigma/\sigma$, where σ is ionic conductivity (Chen *et al.* 2005; Lin *et al.* 2003). For the stable-flow, area-averaged FASS model of interest here, bulk charge density acts as a source of pressure gradient. In the absence of EOF gradients, this local body force is balanced by viscous stresses (and associated pressure gradients) which are distributed throughout the length of the channel. In this appendix we present a brief scaling argument to justify the

assumption that the effects of electric body forces in the bulk are negligible compared to pressure gradients due to mismatched electro-osmotic flow for our parameter range of interest. Assuming one-dimensional conductivity gradients in a long-thin channel, the *distributed* pressure gradient resulting from *local* bulk liquid electric body forces can be estimated from a global force balance as

$$\frac{\mathrm{d}P_E}{\mathrm{d}x} = \frac{1}{L_T}\int_0^{L_T} \rho_E E \,\mathrm{d}x \tag{A 1}$$

where L_T is the total channel length. The charge density can be related to the electric field using Gauss's law as $\rho_E = -\varepsilon_o\varepsilon_r \mathrm{d}E/\mathrm{d}x$. Substituting into equation (A1),

$$\frac{\mathrm{d}P_E}{\mathrm{d}x} = \frac{1}{L_T}\int_0^{L_T} -\varepsilon_o\varepsilon_r \frac{\mathrm{d}(E^2)}{2\,\mathrm{d}x}\,\mathrm{d}x = \frac{\varepsilon_o\varepsilon_r(E^2(x=L_T) - E^2(x=0))}{2L_T}. \tag{A 3}$$

The electric field can be calculated by enforcing conservation of electromigration current in a system with a step-change in electrical conductivity (Burgi & Chien 1991). Enforcement of this condition leads to the result that the ratio of the electric fields in the low- and high-conductivity regions is equal to γ, the high-to-low conductivity ratio. The distributed pressure gradient due to local bulk charge density is then

$$\frac{\mathrm{d}P_E}{\mathrm{d}x} = \frac{\varepsilon_o\varepsilon_r(\gamma^2-1)E_o^2}{2L_T(1+(\gamma-1)a)^2} \tag{A 4}$$

where a is the fraction of channel occupied by the low-conductivity region, and E_o is applied nominal electric field (applied voltage per unit channel length). The pressure gradient in the stacked sample region due to an EOF mismatch can be estimated using continuity and the momentum equation. For a one-dimensional step change in conductivity, the pressure gradient in the stacked analyte region is simply

$$\frac{\mathrm{d}P_{EOF}}{\mathrm{d}x} = \frac{3E_o(\gamma-1)F v_{EOF}\mu a}{2d^2(1+(\gamma-1)a)}. \tag{A 5}$$

The channel depth is $2d$, the wall EOF mobility is v_{EOF}, and the fluid viscosity is μ. Here we assume a uniform electro-osmotic mobility to simplify the analysis. The ratio of the two pressure gradients is then

$$\Gamma = \frac{\mathrm{d}P_E}{\mathrm{d}x}\Big/\frac{\mathrm{d}P_{EOF}}{\mathrm{d}x} = \frac{\varepsilon_o\varepsilon_r E_o\,(\gamma-1)d^2}{3F v_{EOF}\mu a L_T(1+(\gamma-1)a)}. \tag{A 6}$$

Γ is of order 10^{-4} for typical FASS experiment values with significant electro-osmotic mobility (e.g. $E_o = 60\,000\ \mathrm{V\,m^{-1}}$, $L_T = 0.085\ \mathrm{m}$, $v_{EOF} = 5\times10^{-13}\ \mathrm{mol\,N^{-1}\,m\,s^{-1}}$, $d = 10\times10^{-6}\ \mathrm{m}$, $\gamma = 10$, $\varepsilon_o\varepsilon_r = 7\times10^{-10}\ \mathrm{F\,m^{-1}}$ and $a = 0.94$). Under suppressed EOF conditions, with an order-of-magnitude reduction in EOF mobility, Γ is of order 10^{-3}. Thus, pressure gradients in the channel due to space charge density can be neglected in the momentum equation (2.3). This leads to a greatly simplified analysis of the flow field.

REFERENCES

Anderson, J. L. & Idol, W. K. 1985 Electroosmosis through pores with nonuniformly charged walls. *Chem. Engng Commun.* **38**, 93–106.

Aris, R. 1956 On the dispersion of a solute in a fluid flowing through a tube. *Proc. R. Soc. Lond.* A **235**, 67–77.

Bharadwaj, R., Santiago, J. G. & Mohammadi, B. 2002 Design and optimization of on-chip capillary electrophoresis. *Electrophoresis* **23**, 2729–2744.

Bier, M., Palusinski, O. A., Mosher, R. A. & Saville D. A. 1983 Electrophoresis: Mathematical modeling and computer simulation. *Science* **219**, 1281–1287.

Brenner, H. & Edwards, D. A. 1993 *Macrotransport Processes.* Butterworth-Heinemann, Boston.

Burgi, D. S., & Chien, R. L. 1991 Optimization of sample stacking for high performance capillary electrophoresis. *Anal. Chem.* **63**, 2042–2047.

Chen, C.-H., Lin, H., Lele, S. K. & Santiago, J. G. 2005 Convective and absolute electrokinetic instability with conductivity gradients. *J. Fluid Mech.* **524**, 263–303.

Chien, R. L. & Burgi, D. S. 1991 Field amplified sample injection in high-performance capillary electrophoresis. *J. Chromatogr.* **559**, 141–152.

Chien, R. L. & Burgi, D. S. 1992 Sample stacking of an extremely large injection volume in high-performance capillary electrophoresis. *Anal. Chem.* **64**, 1046–1050.

Dutta, D. & Leighton, D. T. 2001 Dispersion reduction in pressure-driven flow through microetched channels. *Anal. Chem.* **73**, 504–513.

Grushka, E., McCormick, R. M. & Kirkland, J. J. 1989 Effect of temperature-gradients on the efficiency of capillary zone electrophoresis separations. *Anal. Chem.* **61**, 241–246.

Horvath, J. & Dolnik, V. 2001 Polymer wall coatings for capillary electrophoresis. *Electrophoresis* **22**, 644–655.

Hunter, R. J. 1981 *Zeta Potential in Colloidal Science: Principles and Applications.* Academic.

Jung, B., Bharadwaj, R. & Santiago, J. G. 2003 Thousand-fold signal increase using field amplified sample stacking for on-chip electrophoresis. *Electrophoresis* **24**, 3476–3483.

Kohlrausch, F. 1897 Ueber concentrations-verschiebungen durch electrolyse im innern von lösungen und lösungsgemischen. *Ann. Physik.* **62**, 209–239.

Levich, B. 1942 The theory of concentration polarization. *Acta Physicochim. URSS* **17**, 257–307.

Lichtenberg, J., Verpoorte, E. & Rooij, N. F. 2001 Sample preconcentration by field amplification stacking for microchip-based capillary electrophoresis. *Electrophoresis* **22**, 258–271.

Lin, H., Storey, B. D., Oddy, M. H., Chen, C.-H. & Santiago, J. G. 2003 Instability of electrokinetic microchannel flows with conductivity gradients. *Phys. Fluids* **16**, 1922–1935.

Mikkers, F. E. P., Everaerts, F. M. & Verheggen, Th. P. E. M. 1979 Concentration distributions in free zone electrophoresis. *J. Chromatogr.* **169**, 1–10.

Preisler, J. & Yeung, E. S. 1996 Characterization of nonbonded poly(ethylene oxide) coating for capillary electrophoresis via continuous monitoring of electroosmotic flow. *Anal. Chem.* **68**, 2885–2889.

Probstein, R. F. 1994 *Physicochemical Hydrodynamics.* John Wiley & Sons.

Sadr, R., Yoda, M., Zheng, Z. & Conlisk, A. T. 2004 An experimental study of electro-osmotic flow in rectangular microchannels. *J. Fluid Mech.* **506**, 357–367.

Santiago, J. G. 2001 Electroosmotic flows in micro-channels with finite inertial and pressure forces. *Anal. Chem.* **73**, 2353–2365.

Sauber, S. G., Locke, B. R. & Arce, P. 1995 Effects of axial and orthogonal applied electric field on solute transport in Poiseuille flows: an area averaging approach. *Ind. Engng Chem. Res.* **34**, 886–894.

Saville, D. A. 1990 The effects of electroosmosis on the structure of isotachophoresis boundaries. *Electrophoresis* **11**, 899–902.

Scales, P. J., Grieser, F. & Healy, T. W. 1992 Electrokinetics of the silica-solution interface: A flat plate streaming potential study. *Langmuir* **8**, 965–974.

Sounart, T. L. & Baygents, J. C. 2001 Electrically-driven fluid motion in channels with streamwise gradients of the electrical conductivity. *Colloid Surf.* A **195**, 59–75.

Stone, H. A. & Brenner, H. 1999 Dispersion in flows with streamwise variations of mean velocity: Radial flow. *Ind. Engng Chem. Res.* **38**, 851–854.

Taylor, G. I. 1953 Dispersion of soluble matter in solvent flowing slowly through a tube. *Proc. R. Soc. Lond.* A **219**, 186–203.

Yang, H. & Chien, R.-L. 2001 Sample stacking in laboratory-on-a-chip devices. *J. Chromatogr.* A **924**, 155–163.

Yao, S., Hertzog, D. E., Zeng, S., Mikkelsen, J. C. & Santiago, J. G. 2003 Porous glass electroosmotic pumps: Design and experiments. *J. Colloid Interface Sci.* **268**, 143–153.